Inferring core-collapse supernova physics with gravitational waves

J. Logue,[1,2,*] C. D. Ott,[3,4,5,†] I. S. Heng,[1,‡] P. Kalmus,[2,3,§] and J. H. C. Scargill[6,2,‖]

[1]*SUPA, Institute for Gravitational Research, School of Physics and Astronomy, University of Glasgow, Glasgow G12 8QQ Scotland*

[2]*LIGO Laboratory, California Institute of Technology, Pasadena, California 91125, USA*

[3]*TAPIR, MC 350-17, California Institute of Technology, Pasadena, California 91125, USA*

[4]*Institute for the Physics and Mathematics of the Universe (IPMU), The University of Tokyo, Kashiwa, Japan*

[5]*Center for Computation and Technology, Louisiana State University, Baton Rouge, Louisiana, USA*

[6]*New College, Oxford, OX1 3BN, United Kingdom*

(Received 23 February 2012; published 17 August 2012)

Stellar collapse and the subsequent development of a core-collapse supernova explosion emit bursts of gravitational waves (GWs) that might be detected by the advanced generation of laser interferometer gravitational-wave observatories such as Advanced LIGO, Advanced Virgo, and LCGT. GW bursts from core-collapse supernovae encode information on the intricate multidimensional dynamics at work at the core of a dying massive star and may provide direct evidence for the yet uncertain mechanism driving supernovae in massive stars. Recent multidimensional simulations of core-collapse supernovae exploding via the neutrino, magnetorotational, and acoustic explosion mechanisms have predicted GW signals which have distinct structure in both the time and frequency domains. Motivated by this, we describe a promising method for determining the most likely explosion mechanism underlying a hypothetical GW signal, based on principal component analysis and Bayesian model selection. Using simulated Advanced LIGO noise and assuming a single detector and linear waveform polarization for simplicity, we demonstrate that our method can distinguish magnetorotational explosions throughout the Milky Way ($D \lesssim 10$ kpc) and explosions driven by the neutrino and acoustic mechanisms to $D \lesssim 2$ kpc. Furthermore, we show that we can differentiate between models for rotating accretion-induced collapse of massive white dwarfs and models of rotating iron core collapse with high reliability out to several kpc.

DOI: 10.1103/PhysRevD.86.044023 PACS numbers: 04.30.Tv, 04.80.Nn, 05.45.Tp, 97.60.Bw

I. INTRODUCTION

Almost eighty years after the proposal by Baade and Zwicky that (core-collapse) supernovae represent the transition of an ordinary massive star into a neutron star [1], we still lack a complete understanding of this phenomenon. In particular, we do not know with certitude how the *supernova mechanism* operates and converts the necessary fraction of gravitational energy of collapse into kinetic energy and light of the explosive outflow.

The basic story line of core collapse goes as follows (see [2,3] for detailed reviews): At the end of a massive star's ($8\text{–}10M_\odot \lesssim M \lesssim 130M_\odot$ at zero-age main sequence [ZAMS]) life, nuclear burning has ceased in its core, which is then composed primarily of iron-group nuclei (or O − Ne nuclei at the lower end of the mass range) and supported against gravity by the pressure of relativistically degenerate electrons. Eventually, the core exceeds its effective Chandrasekhar mass and dynamical collapse sets in. The collapsing core separates into subsonically infalling homologous ($v \propto r$) inner core and supersonically collapsing outer core [4,5]. When the inner core reaches nuclear density, the repulsive core of the nuclear force leads to a stiffening of the nuclear equation of state (EOS). The inner core, suddenly supported by the stiff supernuclear EOS, overshoots its new equilibrium, then bounces back into the still infalling outer core. A shock wave forms at the sonic point between inner and outer core at an enclosed baryonic mass of $\sim 0.5M_\odot$. It quickly moves out in radius and mass, but must do work in breaking up infalling iron-group nuclei. This and neutrino losses from electron capture in the region behind the shock sap its might. The shock succumbs to the ram pressure of the outer core, stalls, and turns into an accretion shock.

The shock must be reenergized to drive a core-collapse supernova explosion and, in the canonical scenario, leave behind a neutrino-cooling and contracting protoneutron star. This shock revival must, depending on progenitor star structure, occur within ~0.5–3 s, otherwise accretion will push the protoneutron star over its maximum mass, leading to collapse and black hole formation [6]. Understanding the supernova mechanism, which must robustly revive the stalled shock in supernovae from massive stars that are observed on a daily basis, is the principle current challenge of core-collapse supernova theory.

*j.logue@physics.gla.ac.uk
†cott@tapir.caltech.edu
‡ik.heng@glasgow.ac.uk
§kalmus@caltech.edu
‖james.scargill@new.ox.ac.uk

Observational clues for the supernova mechanism are few. Electromagnetic waves are emitted in optically thin regions far from the core and thus yield only second-hand information about the supernova mechanism. Yet, observations of ejecta morphology, spatial distributions of nucleosynthetic yields, and pulsar kicks are indicative of aspherical (i.e., multidimensional) processes bearing relevance in the explosion dynamics (e.g., [7,8], and references therein). Neutrinos, on the other hand, are emitted deep inside the core and can provide crucial thermodynamic, structural, and, to some extent, dynamical information on what occurs in the core [2,9,10]. The few neutrinos captured from supernova 1987A [2,11] have impressively confirmed the very basic picture of core collapse outlined in the above.

Gravitational waves (GWs), like neutrinos emitted from dense regions impenetrable by photons, carry dynamical information about their source. Since their emission occurs at lowest order by accelerated quadrupole motions, GWs are direct probes of multidimensional dynamics in the core that may play a crucial role in the supernova mechanism [3,12].

Stellar collapse has long been considered a promising source of GWs for detectors on Earth (see the historical overview in [12]) and much effort has gone into understanding the GW signature of stellar collapse and the subsequent evolution towards a core-collapse supernova explosion. This has led to the identification of a range of emission processes, including rotating collapse and core bounce, nonaxisymmetric rotational instabilities, aspherical outflows, convection/turbulence in the protoneutron star and in the region immediately behind the shock, instabilities of the standing accretion shock, pulsations of the protoneutron star, asymmetric emission of neutrinos, and magnetic stresses (see [12,13] for recent reviews). The most recent set of simulations [12,14–19] suggests that GWs from the average core-collapse supernova may be visible throughout the Milky Way for the second generation of laser interferometer GW observatories, including Advanced LIGO, Advanced Virgo, and LCGT [20,21]. Extreme emission scenarios may allow detection throughout the local group of galaxies, including the Andromeda galaxy [12,22–24], but third-generation detectors such as the Einstein Telescope [25] might hope to observe more distant events.

If it was possible to associate an explosion mechanism with particular multidimensional dynamics that leads to a characteristic GW signal, then the detection or nondetection of such a signal from the next galactic core-collapse supernova could confirm or rule out this mechanism. To realize such a GW-observational test of the explosion mechanism, one must separate the signal from detector noise and determine its parameters, e.g., by matching, in some way, to signal predictions from simulations. The most straightforward method for signal extraction and parameter estimation is matched filtering (e.g., [26]), which looks for a match of detector data with waveform templates from simulations. Matched filtering requires exact knowledge of the expected signal, which is possible, e.g., for the inspiral phase of compact binaries, since the parameter space of binary systems is limited, all relevant physics is understood (at least in the black-hole-black-hole binary case) and numerical relativity simulations can predict essentially exact waveform templates (i.e., limited only by numerical error). However, building waveform catalogs with exact predictions for matched filtering is impossible for GWs from core-collapse supernovae. On the one hand, there is unknown physics (e.g., the nuclear EOS) and many unconstrained parameters (e.g., the details of the precollapse configuration are poorly known) in the stellar collapse problem. This alone would require extensive parameter studies to build up template databases covering the poorly constrained parameter space. On the other hand, all expected GW emission processes in core-collapse supernovae are influenced or dominated by turbulent flow. Hence, their GW signals have a stochastic component that is impossible to predict, even if all initial conditions and physics were known exactly. Matched filtering is not applicable to such GW bursts. To extract the GW signal from the next galactic core collapse event and determine source physics such as the explosion mechanism, an approach to signal extraction/reconstruction, model selection, and parameter estimation is needed that can handle the stochastic nature of the expected GW signals.

The reconstruction of both polarizations of a GW signal requires coincident observations of two detectors; linearly polarized signals can be reconstructed from data of just one detector and adding a third detector overdetermines the problem, permitting the source position on the sky to be determined [27]. GW signal reconstruction was pioneered by Gürsel and Tinto [28] with a maximum likelihood approach, variants [29,30] of which have been incorporated into search pipelines for GW bursts [31].

Summerscales *et al.* [32] were the first to study signal reconstruction and parameter estimation for the GW burst from rotating core collapse and bounce based on waveforms of Ott *et al.* [33]. They injected signals into real detector noise of early LIGO science runs and used a maximum entropy approach to reconstruct the signal using data from two detectors without any a priori knowledge of the signal shape. Cross correlation of the reconstructed signal with signal predictions of [33] was then used to determine source parameters.

Incorporating GW signal information from core collapse simulations into detection and signal reconstruction approaches was first considered by Brady and Ray-Majumder [34], who realized that the GW burst from rotating collapse and bounce, while being unpredictable

in detail, has robust features that can be isolated mathematically. They created an orthonormal vectorspace of waveforms from [33,35] using Gram-Schmidt orthonormalization and isolated a subspace of essential features most common to all waveforms. Heng [36] also considered waveforms from rotating core collapse and bounce and utilized the more recent waveform catalog of Dimmelmeier *et al.* [17]. He performed principal component analysis (PCA; e.g., [37]), which transforms a correlated, multidimensional data set into a set of orthogonal components by determining the eigenvectors and eigenvalues of the covariance matrix of the data set. The principal component (PC) vectors are the eigenvectors ranked according to their corresponding eigenvalue, with the first PC being the eigenvector with the largest eigenvalue. Cannon *et al.* [38] have also utilized this method for GW signals from compact binary coalescence.

Röver *et al.* [39] went a step further and combined PCA with Bayesian inference using the Markov chain Monte Carlo technique for computing marginalization integrals (see, e.g., [40] for a pedagogical introduction to Bayesian methods). They considered linearly-polarized waveforms from rotating core collapse and bounce and were able to reconstruct signals from modeled noise in a single detector and infer key parameters, e.g., the nuclear EOS used in the simulation that led to a given trial waveform.

In this paper, we present a proof-of-principle study to demonstrate that the core-collapse supernova explosion mechanism can be inferred from the GW signal of a galactic core-collapse supernova observed with second-generation GW observatories such as Advanced LIGO, Advanced Virgo, and LCGT. We consider the neutrino mechanism (e.g., [3]), the magnetorotational mechanism (e.g., [41]), and the acoustic mechanism [42,43], discuss their essentials, and argue that they bear distinct GW signatures as first pointed out by Ott [12,44], which is a prerequisite for our study. We follow the approach of Röver *et al.* [39] and, for simplicity, restrict ourselves to a single detector, linearly polarized signals, and a Gaussian noise model at the noise level of Advanced LIGO in broadband mode. Like Röver *et al.*, we adopt a Bayesian approach and use PCA, but, for the first time, apply it to multiple waveform catalogs. We associate each waveform catalog with one of the three mechanisms and calculate Bayes evidence ratios using the nested sampling algorithm [40,45] to determine what mechanism's PCs match best with a given injected signal. We demonstrate that this approach can identify any of the considered explosion mechanisms with high confidence for core collapse events occurring at distances of up to $\sim$2 kpc. The magnetorotational explosion mechanism can even be inferred throughout the Milky Way ($D \gtrsim 10$ kpc). In addition to studying the explosion mechanism, we also consider the problem of determining whether a core-collapse event is a rapidly rotating ordinary iron core collapse or an accretion-induced collapse (AIC) of a massive white dwarf. These two processes are governed by the same physics and differences in their waveforms are subtle [46], but our approach is still capable of telling them apart.

This article is structured as follows: Sec. II reviews the set of considered candidate core-collapse supernova mechanisms, their individual GW signatures, and the GW signal catalogs that we draw model waveforms from. In Sec. III, we introduce our method for model selection via PCA and nested sampling. The results of our study are presented and discussed in detail in Sec. IV. We summarize and conclude in Sec. V.

II. SUPERNOVA MECHANISMS AND THEIR GRAVITATIONAL WAVE SIGNATURES

In this study, we consider the neutrino mechanism, the magnetorotational mechanism, and the acoustic mechanism for core-collapse supernova explosions and describe them and their characteristic GW signal features in the following sections. Variations of these mechanisms and alternatives have been discussed elsewhere (e.g., [3,47]).

A. Neutrino mechanism

The gravitational collapse of the iron core and the subsequent evolution of the nascent hot puffed-up proto-neutron star to a cold compact neutron star release of order 300 B (1 Bethe $= 10^{51}$ erg) of energy, $\sim$99% of which is emitted in the form of neutrinos of all flavors [2]. If only a small fraction of the energy released in neutrinos is reabsorbed behind the stalled shock, leading to net heating, an explosion could be launched and endowed with the energy to account for the observed range of asymptotic explosion energies of 0.1–1 B of garden-variety core-collapse supernovae [48]. This is the gist of the neutrino mechanism of core-collapse supernovae, which, in its early form was proposed by Arnett [49] and Colgate and White [50], and in its modern form by Bethe and Wilson [51].

Despite its appealing simplicity, the neutrino mechanism, in its purest, spherically-symmetric (one-dimensional) form, fails to revive the shock in all but the lowest-mass massive stars with O $-$ Ne cores [52–55]. There is now strong evidence from axisymmetric [two-dimensional (2D)] [14,19,56–60] and first three-dimensional (3D) [15,16,61–66] simulations that the breaking of spherical symmetry is key to the success of the neutrino mechanism. In 2D and 3D, neutrino-driven convection in the region of net heating behind the shock, and the standing-accretion-shock instability (SASI) [67–70] increase the efficiency of the neutrino mechanism [60,62,63,65].

Leaving rapid rotation aside for a moment, the dominant multidimensional GW-emitting dynamics in neutrino-driven core-collapse supernovae are convection in the protoneutron star (e.g., [71,72]) and SASI-modulated

convection in the region behind the stalled shock. GW emission from convection and SASI has been extensively studied in simulations in 2D [58,71–74] and to some extent in 3D [15,16,75,76]. The top panel in Fig. 1 shows a typical example waveform drawn from the catalog of Murphy *et al.* [73]. Right after core bounce, an initial burst of GWs is emitted by strong, so-called prompt convection [12], driven by the negative entropy gradient left behind by the stalling shock. Subsequently, the GW signal settles at lower amplitudes, then picks up again as the SASI reaches its nonlinear phase and high-velocity accretion

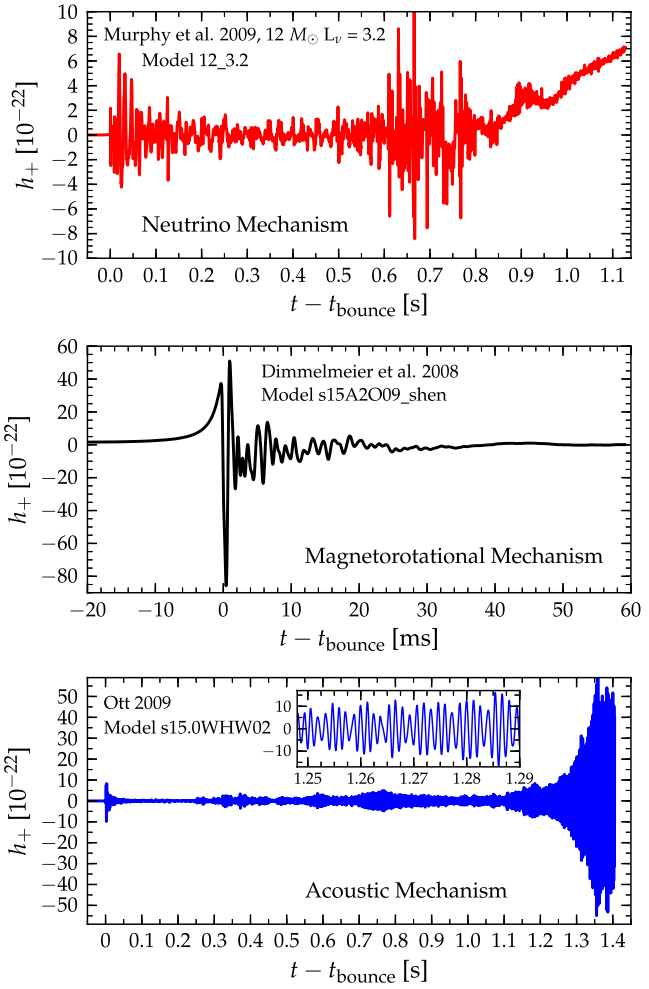

FIG. 1 (color online). Linearly polarized GW signal predictions for a core collapse event located at 10 kpc from matter dynamics in axisymmetric simulations that can be associated with the neutrino mechanism (top panel, taken from [73]), the magnetorotational mechanism (center panel, taken from [17]), and the acoustic mechanism (bottom panel, taken from [12]). Note the varying ranges of the time and strain axes. Also note that the simulations of [17] did not include magnetic fields, since the GW signal from core bounce in magnetorotational explosions is due to rapid rotation and not influenced by magnetic fields. This, however, did not allow them to capture the expected secular rise of the waveform expected to occur once an explosion sets in [18]. See text for further discussion.

downstreams penetrate deep into the region behind the shock, where they are decelerated, leading to pronounced spikes in the wave signal [73]. The secular rise in the signal amplitude towards the end of the waveform is due to the onset of an aspherical explosion [15,58,73], but occurs at too low characteristic frequencies to be visible to Advanced LIGO-class detectors. Not included in the top panel of Fig. 1 is the contribution to the GW signal from anisotropic neutrino emission [77–79], which can dominate in amplitude, but, like the contribution from aspherical outflow, occurs on time scales too long to lead to emission at frequencies detectable by the upcoming generation of ground-based detectors [15,16,58,71,74,76].

Overall, the detectable GW signal from a neutrino-driven nonrotating or slowly rotating core-collapse supernova will have random polarization, a broadband spectrum from ~100–1000 Hz and typical strain amplitudes $|h|$ of order $10^{-22}(D/10\ \mathrm{kpc})^{-1}$, with individual peaks reaching $10^{-21}(D/10\ \mathrm{kpc})^{-1}$ [12,15]. The typical duration of emission is the time from core bounce to the launch of the explosion, 0.3–1 S, but convection inside the cooling protoneutron star can continue to emit GWs at lower amplitudes and higher frequencies for many seconds afterwards [12,71]. Typical total emitted GW energies are in the range 10^{-11}–$10^{-9} M_\odot c^2$ [12,58,73].

The effects of rotation on the neutrino mechanism and its GW signature are not yet fully understood (see, e.g., [14,19,44,57,59,80,81]) and it cannot be excluded that contributions from rotational dynamics may modify the GW signal of neutrino-driven core-collapse supernovae. However, results from the systematic rotating core-collapse studies of [17,18,41,81] suggest that once rotation rates become sufficiently high to alter the dynamics, the explosion is actually more likely to occur via the magnetorotational mechanism discussed in Sec. II B. This, however, is under the provision that the magnetorotational instability (e.g., [82,83]) works robustly and builds up the required strong magnetic fields to drive an explosion.

Keeping the above caveats in mind, for the purpose of this study, we make the assumption that the GW signature of neutrino-driven core-collapse supernovae is unaffected by rotational effects.

1. GW signal catalogs

In this study, we use the catalog of Murphy *et al.* [73], which is available for download from [84]. The Murphy *et al.* catalog (in the following, we refer to waveforms from this catalog as MUR waveforms) encompasses 16 waveforms that were extracted via the quadrupole formula (e.g., [85]) from Newtonian axisymmetric core-collapse simulations that used a parametrized scheme for electron capture and neutrino heating/cooling and included only the monopole component of the gravitation potential as described in [60,73]. The Murphy *et al.* simulations are nonrotating and the parameter space covered is spanned by progenitor

ZAMS mass ({12, 15, 20, and 40} $M_\odot$) and by the dialed-in total electron and antielectron neutrino luminosity.

Yakunin *et al.* [58] performed self-consistent axisymmetric Newtonian (with an approximate-GR monopole term of the gravitational potential [86]) radiation-hydrodynamics simulations of neutrino-driven core-collapse supernovae. They provide three waveforms at [87], obtained from simulations using progenitors of (12, 15, and 25) $M_\odot$. We use the Yakunin waveforms (denoted, in the following, as YAK waveforms) to test the robustness of our supernova mechanism determination algorithm, which uses the PCs of the MUR waveforms.

Since we are limiting ourselves to one detector in this proof-of-principle study, we are considering only linearly polarized signals. Gravitational waveforms with $+$ and $\times$ polarizations from 3D simulations of neutrino-driven core-collapse supernovae [15,16,76] will be considered in future work.

B. Magnetorotational mechanism

The conservation of angular momentum in core collapse to a protoneutron star leads to a spin-up by a factor of $\sim$1000 [88]. Starting from a precollapse angular velocity distribution that may be expected to be more or less uniform in the inner core (e.g., [89]), homologous collapse preserves the uniform rotation of the inner core while the supersonic collapse of the outer core leads to strong differential rotation in the outer protoneutron star and in the region between protoneutron star and shock [88].

A rapidly spinning precollapse core with a period of order 1 s results in a ms-period protoneutron star, with a rotational energy of order 10 B, which is about ten times greater than the typical core-collapse supernova explosion energy. If only a fraction of this energy was tapped, a strong explosion could be triggered.

Theory and simulations (e.g., [18,41,90–96]) have shown that magnetorotational processes are efficient at extracting spin energy and can drive collimated outflows, leading to energetic bipolar jet-like explosions. Recent work [18,41,94–96] suggests that magnetic fields of the order of 10^{15} G with strong toroidal components are required to yield the necessary magnetic stresses to drive a strong bipolar explosion. If 10^{15} G fields were to arise from flux compression in collapse alone, precollapse core fields would have to be of order 10^{12} G [41,94], which is about 3 orders of magnitude larger than predicted by stellar evolution models (e.g., [89,97]). It is more likely that the most significant amplification occurs after core bounce via rotational winding of poloidal into toroidal field (a linear process), the nonlinear magnetorotational instability (MRI, which is not yet fully understood in the core-collapse context [82,83]). Both processes operate on the free energy stored in differential rotation, which is abundant in the outer core.

For the magnetorotational mechanism to work, precollapse spin periods $\lesssim$ 4–5 s appear to be required [41]. Such rapid rotation leads to a strongly centrifugally-deformed inner core with a large quadrupole moment ($\ell = 2$; due to its oblateness), which rapidly changes during core bounce, leading to a strong burst of GWs. The GW signal from rotating collapse and bounce has been studied extensively and the most recent general-relativistic simulations have shown it to be of rather generic morphology with a single strong peak at bounce and a subsequent ringdown as the protoneutron star core settles into its new equilibrium [17,98,99]. A typical example GW signal taken from the catalog of Dimmelmeier *et al.* [17,100] is shown in the center panel of Fig. 1. The core-collapse and bounce phase proceeds essentially axisymmetrically even in very rapidly spinning cores [99,101,102] and its GW signal is linearly polarized with vanishing amplitude seen by an observer located along the symmetry axis and maximum amplitude for an equatorial observer. Typical emission durations for the linearly polarized GWs from core bounce are of order 10 ms and peak GW amplitudes for rapidly spinning cores that may lead to magnetorotational explosions are of order 10^{-21}–10^{-20} at 10 Kpc with most of the energy being emitted around 500–800 Hz in cores that reach nuclear density and bounce due to the stiffening of the nuclear EOS. Cores with initial spin periods shorter than $\sim$0.5–1 s experience a slow bounce at sub-nuclear densities strongly influenced or dominated by the centrifugal force. They emit most of the GW energy at frequencies below $\sim$200 Hz [12,17]. Typical emitted GW energies are in the range 10^{-10}–$10^{-8} M_\odot c^2$. The GW signal from rotating collapse and core bounce is unlikely to be affected by MHD effects, since the build up to dynamically relevant field strengths occurs only after bounce [18,41,92,93].

Due to the strong rotational deformation of the protoneutron star, neutrinos decouple from the matter at smaller radii and hotter temperatures in polar regions than near the equator. This leads to the emission of a larger neutrino flux with a harder neutrino spectrum in polar regions (e.g., [59]). This globally asymmetric neutrino emission results in a secularly rising low-frequency GW signal [12]. Similar low-frequency contributions will come from the bipolar outflow characteristic for a magnetorotational explosion and from magnetic stresses [18,92,93]. The low-frequency waveform components are not shown in the center panel of Fig. 1 and are not detectable by the upcoming second-generation earthbound GW observatories.

Also associated with rapid rotation and the magnetorotational mechanism are rotational instabilities that may lead to nonaxisymmetric deformations of the protoneutron star whose "bar-mode" ($m = 2$) components may emit elliptically polarized GWs for tens to hundreds of milliseconds [99,101–104]. However, these instabilities, and in particular their interplay with magnetic fields and the MRI (see, e.g., [105]), are not yet fully understood. Since we are considering only linearly polarized signals and are limited to one detector, we do not include GW signals from these nonaxisymmetric instabilities in this study.

1. GW signal catalogs

We employ the large (128 waveforms) GW signal catalog of Dimmelmeier *et al.* [17,100] (DIM in the following), who performed 2D GR simulations of rotating iron core collapse for (11.2, 15, 20, and 40) $M_\odot$ progenitors and two different nuclear EOS, varying initial rotation rate and degree of differential rotation. They approximated the effects of electron capture during collapse by parametrizing the electron fraction Y_e as a function of density, which yields inner core sizes that are very close to those obtained with full neutrino transport [106]. The inner core size determines the amount of mass and angular momentum that can be dynamically relevant during core bounce and, hence, is a determining factor in the GW signal [98]. The DIM catalog was also used by the previous parameter estimation work of Röver *et al.* [39]. For testing, we use the three additional DIM waveforms computed for [39] that are not part of the original DIM catalog and were used to test their algorithm. We label this set of extra waveforms as DIMEXTRA.

For studying the robustness of our mechanism-determination approach, we draw gravitational waveforms of rotating models from the catalog of Scheidegger *et al.* [102,107], (SCH in the following) who performed 3D Newtonian-MHD rotating iron core-collapse calculations with a spherical approximate-GR gravitational potential and employed the same EOS and electron capture treatment as Dimmelmeier *et al.* [17], but used different progenitor models.

Furthermore, we use the GW signal catalog of Abdikamalov *et al.* [46,84] (ABD in the following) who used the same numerical code as Dimmelmeier *et al.* [17], but studied the rapidly spinning AIC of massive white dwarfs to neutron stars. This process yields a GW signal very similar to rotating iron core collapse and explosions in AIC may occur also via the magnetorotational mechanisms [108]. We include this catalog of 106 waveforms to see if our algorithm can differentiate between rotating iron core collapse and rotating AIC assuming the DIM and ABD catalogs correctly predict the respective GW signals.

C. Acoustic mechanism

The core-collapse supernova evolution in the *acoustic mechanism* proposed by Burrows *et al.* [22,42,43] is initially identical to the one expected for the neutrino mechanism. Neutrino heating, convection, and the SASI set the stage, but no explosion is triggered for $\gtrsim 500$ ms after bounce. At this point, the SASI is in its highly nonlinear phase and modulates high-velocity accretion downflows that impact on the protoneutron star and excite core pulsations (primarily $\ell = \{1, 2\}$ g modes). Over hundreds of milliseconds, these pulsations reach large amplitudes and damp via the emission of strong sound waves. Traveling down the steep density gradient in the region behind the shock, the sound waves steepen to shocks and dissipate their energy behind and in the shock. This mechanism is robust in the simulations by Burrows *et al.* [22,42,43], but requires $\gtrsim 1$ s to develop, thus leads to massive NSs, and tends to yield explosion energies on the lower side of what is observed.

The GW signature of the acoustic mechanism is dominated by the strong emission from the quadrupole components of the protoneutron star core pulsations that are quasi-periodic (their frequency shifts secularly along with the changing protoneutron star structure) and become very strong $\gtrsim$ 800–1000 ms after core bounce [12,22]. The lower panel of Fig. 1 depicts a typical example waveform from Ott *et al.* [12,22], who studied the GW signature of the acoustic mechanism based on the simulations of Burrows *et al.* [42,43]. At early times, the GW signal is essentially the same as expected for the neutrino mechanism, but once the protoneutron star core pulsations grow strong, they are hard to miss. The simulations of Burrows *et al.* [22,42,43] were axisymmetric and the resulting GW signals are linearly polarized, though in 3D, one would expect oscillation power also in nonaxisymmetric components. Typical maximum strain amplitudes are of order few $\times 10^{-21}$–10^{-20} and multiple modes with frequencies between $\sim$600–1000 Hz contribute to the emission. Since the pulsations last for many cycles, the emitted GW energies may be large and are predicted to be of order 10^{-8}–$10^{-7} M_\odot c^2$ and extreme models reach few $\times 10^{-5} M_\odot c^2$ [12,22].

There are multiple caveats associated with the acoustic mechanism that must be mentioned. Most importantly, the acoustic mechanism has been found in simulations of only one group with a single simulation code, but others have not yet ruled out the possibility of strong protoneutron star pulsations at late times (e.g., [19]). In a nonlinear perturbation study, Weinberg and Quataert [109] found that the protoneutron star pulsation amplitudes may be limited by a parametric instability involving high-order modes that damp efficiently via neutrino emission and are not presently resolved in numerical simulations. This would limit the protoneutron star pulsations to dynamically insignificant amplitudes. Moreover, the simulations of Burrows *et al.* were axisymmetric and nonrotating or only very slowly rotating. It is not clear to what amplitudes individual protoneutron star pulsation modes would grow in 3D. Rapid rotation, due to its stabilizing effect on convection and SASI [44,59], may likely inhibit the growth of pulsations. Both 3D and rotational effects remain to be explored.

1. GW signal catalogs

We employ the set of 7 waveforms from the models of [43] analyzed by Ott [12] and available at [84]. We refer to this set as the OTT catalog in the following and use them to compute PCs for the acoustic mechanism's GW signature. All waveforms were computed on the basis of the Burrows *et al.* [22,42,43] simulations and differ only in the

employed progenitor model, covering a range in ZAMS mass from 11.2 to $25M_\odot$.

Three additional waveforms of an earlier study of Ott *et al.* [22] are available [84]. We label this small set OTTEXTRA and use them for testing our method's capability of correctly identifying them as coming from stars exploding via the acoustic mechanism.

III. DATA ANALYSIS

A. Strategy

The three example gravitational waveforms shown in Fig. 1 that are associated with the three supernova mechanisms are clearly different. Provided the assumptions made in associating these signals with the various mechanisms are correct, a GW signal detected from a core-collapse supernova should, in principle, allow to determine the explosion mechanism. To do so in practice, two problems most be overcome: (i) The exact waveform of an incident signal is impossible to predict in advance. (ii) Real GW detectors are noisy instruments (see, e.g., [110] for a discussion of detectors and noise sources) and any GW signal will be contaminated by detector noise. In other words, it is necessary to develop a data analysis algorithm that is capable of distinguishing between underlying physical models (e.g., supernova mechanisms) on the basis of a noisy signal whose detailed shape cannot be predicted exactly.

In the following subsections, we describe the components of a Bayesian data analysis algorithm which classifies detected GW signals from core-collapse supernovae as belonging to one of a set of signal catalogs, representing, e.g., different explosion mechanisms. A block diagram of the analysis algorithm, which we call the supernova model evidence extractor (SMEE), is shown in Fig. 2. SMEE is implemented in MATLAB.[1]

In a first step, SMEE performs PCA via SVD on the waveforms in each catalog to create sets of orthogonal basis vectors, the PCs, which are ordered according to their prevalence in their catalog. In other words, the first PC represents the most common feature of all signals in the catalog, the second PC represents the second most common feature, and so on. Using a complete set of PCs, each waveform can be reconstructed as a linear combination of PCs for the corresponding catalog, allowing each waveform to be simply parametrized by the PC coefficients in the linear combination. However, since PCs are expected to span the parameter space defined by each catalog of waveforms efficiently, catalog waveforms may be reconstructed with good accuracy already with a set of PCs that is significantly smaller than the number of waveforms in the catalog. Moreover, noncatalog waveforms (i.e., real signals) may be identified as belonging to the same class of signals as catalog waveforms if they can be approximately matched with the first few PCs of a catalog.

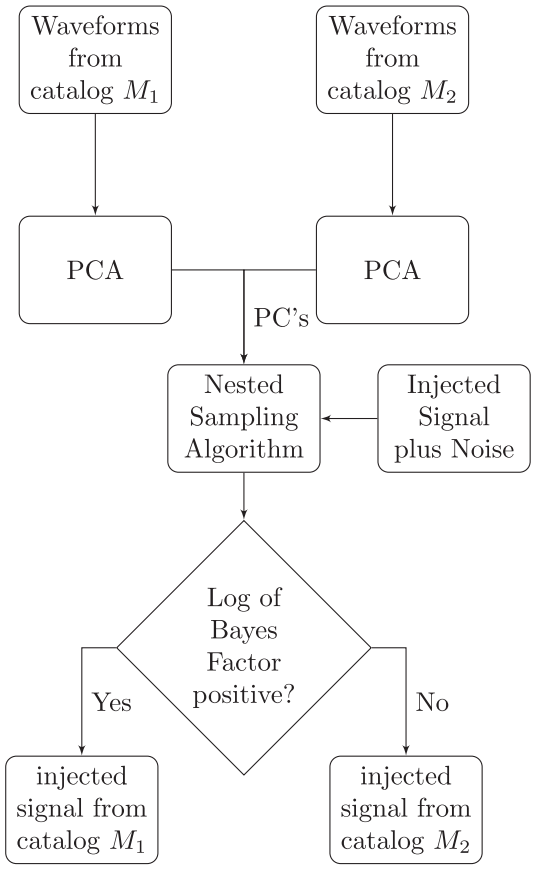

FIG. 2. Block diagram of the SMEE. A desired core-collapse supernova gravitational wave signal is injected into noise, and the algorithm compares it to the PCs of a given waveform catalog representing a particular model. The PCs are constructed via SVD. The sign of the log Bayes factor between two PC sets indicates which model is favored by the data.

SMEE then uses Bayesian model selection and computes the logarithm of the Bayes factor to distinguish between GW signal classes. The Bayes factor is the ratio of the evidences for two competing hypotheses and, for the purpose of our analysis, we weigh the evidence that the observed data supports the presence of a GW signal consistent with signals from one of any two competing catalogs. This requires summing up the likelihood function times the prior across all possible signal parameters (in our case, values of PC coefficients) to determine the evidence (also called the marginal likelihood) for two different signal models to be tested. SMEE accomplishes this efficiently via the nested sampling algorithm [40,45].

B. Bayesian model selection

In our analysis, we employ Bayesian model selection, similar to that described in [111]. Specifically, we use the Bayes factor to compare the probabilities of two competing

[1]The MathWorks Inc., Natick, MA 01760, USA, http://www.mathworks.com/products/matlab/.

models. In general terms, the Bayes factor B_{ij} can be written as the ratio of the evidences $p(D|M)$,

$$B_{ij} = \frac{p(D|M_i)}{p(D|M_j)}, \tag{1}$$

where M_i and M_j are two competing models tested using the data D. The evidence for each model is obtained by integrating the product of its likelihood function, $p(D|\theta, M)$, and prior, $p(\theta|M)$, across all model parameter values θ, such that,

$$p(D|M) = \int_\theta p(\theta|M)p(D|\theta, M)d\theta. \tag{2}$$

This effectively calculates the likelihood averaged over all parameter values. The distribution of the prior reflects our bias for or against particular parameter values. For the analysis discussed in this article, we adopt a flat, uniform prior over all parameter values which means that we do not favour any particular portion of the parameter space.

The evidence will be greater for a model that is supported by the data. Therefore, the Bayes factor indicates which of the two competing models is preferred by the data. It is often more convenient to compare models by using the natural logarithm of the Bayes factor,

$$\log B_{ij} = \log p(D|M_i) - \log p(D|M_j). \tag{3}$$

In this case, $\log B_{ij} > 0$ means M_i is the preferred model, whereas $\log B_{ij} < 0$ will point to M_j being favored.

C. Nested sampling algorithm

For evaluating $\log B_{ij}$, we first need to calculate the evidences $p(D|M_i)$ and $p(D|M_j)$ for the two models M_i and M_j. From Eq. (2), we see that the evidence is the sum of the likelihood times the prior determined for all possible parameter values of the desired model. An exhaustive, brute-force approach to computing the evidence by calculating the likelihood values for every choice of parameter values is computationally prohibitive. It is also an inefficient way of determining the evidence since the likelihood values will be most significant, and therefore contribute most to the evidence, for a small subset of parameter values which constructs a waveform that closely resembles the data. For most other combinations of the model's parameters, the likelihood will be insignificant and do not contribute to the evidence.

Therefore, we choose to follow the approach of Veitch *et al.* [112] and employ nested sampling [40,45] to efficiently calculate the evidence integral. The nested sampling algorithm determines the evidence integral by calculating the likelihood for sample values of the desired model's parameters. Initially, the model's parameter values are randomly selected. The algorithm then iterates over different sets of the model's parameter values, calculating the likelihood for each set of parameter values. With each iteration, the smallest likelihood value obtained is compared with that calculated for a randomly chosen set of new parameter values. Only parameter values which lead to a larger likelihood value than the smallest obtained in the previous iteration are kept. Therefore, as the algorithm stochastically samples the parameter space, it iteratively converges on the set of parameter values that produce the most significant likelihood values.

The nested sampling algorithm is similar to the Markov chain Monte Carlo approach (e.g., [40]) except that the primary output of the nested sampling algorithm is the evidence, which can be immediately obtained by summation, whereas the posterior distribution is only found as a byproduct. To find the evidence, a set of "live points" are found through creating a stochastic sampling of the prior distribution to generate a set of N samples which are denoted as θ_i, where $i = 1 \ldots N$. In context of the analysis presented in later in this article (see Sec. III E), θ_i corresponds to β_i which is the ith sample of the principal component coefficient for which we calculate the signal likelihood. The evidence integral (Eq. (2)) is then written as

$$\begin{aligned} p(D|M) &= \int_\theta p(\theta|M)p(D|\theta, M)d\theta, \\ &\approx \sum_{i=1}^{N} p(D|\theta_i, M)w_i, \approx \sum_{i=1}^{N} L_i w_i, \end{aligned} \tag{4}$$

where the weight,

$$w_i = p(\theta_i|M)d\theta_i, \tag{5}$$

is the fraction of the prior distribution represented by the ith sample and L_i is its likelihood. It is this weighted likelihood that is calculated by the nested sampling algorithm and subsequently used to obtained the evidence. More details on the nested sampling algorithm can be found in [45,112].

D. Principal component analysis via singular value decomposition

Each core-collapse supernova waveform catalog consists of a number of GW signals obtained for different initial conditions and simulation parameters (e.g., progenitor star mass, EOS, rotational configuration, etc.). While individual waveforms of one catalog are different in detail, they generally exhibit strong common general features. This can be exploited by PCA [37], which isolates the most common features of waveforms in linearly independent PCs ordered by their relevance. The first few PCs may already be sufficient to efficiently span their entire catalog, as was shown in [36,39] for the DIM catalog (see Sec. II B 1).

The PCs are obtained via SVD (e.g., [37]) of time-domain waveforms from each catalog. To perform SVD on a catalog with m waveforms, a matrix $\mathbf{A}$ is created such

that each of its columns corresponds to a waveform of uniform length n from the catalog.

The $n \times m$ waveform matrix $\mathbf{A}$ is factored so that

$$\mathbf{A} = \mathbf{U}\mathbf{\Sigma}\mathbf{V}^T, \tag{6}$$

where $\mathbf{U}$ is an $n \times n$ matrix whose columns correspond to the eigenvectors of $\mathbf{A}\mathbf{A}^T$. Similarly, the columns of the $m \times m$ matrix $\mathbf{V}$ correspond to the eigenvectors of $\mathbf{A}^T\mathbf{A}$ and $\mathbf{\Sigma}$ is an $n \times m$ diagonal matrix whose elements correspond to the square root of the corresponding eigenvalues.

Since $\mathbf{A}\mathbf{A}^T$ is the covariance matrix of $\mathbf{A}$, the eigenvectors in $\mathbf{U}$ are effectively an orthonormal basis which span the m-dimensional parameter space defined by the catalog of waveforms used to construct $\mathbf{A}$. Note that, in practice, $n \gg m$ and it is impractical to determine the eigenvectors in $\mathbf{U}$ directly. Instead, the smaller $\mathbf{V}$ and its corresponding eigenvalues in $\mathbf{\Sigma}$ are first determined which are subsequently used to derive $\mathbf{U}$.

The orthonormal eigenvectors of $\mathbf{U}$ are the PCs and are ranked by their corresponding eigenvalues. The PC with the largest corresponding eigenvalue is referred to as the first PC and consists of the most significant common features of all waveforms in the catalog. It follows that the PC with the second largest corresponding eigenvalue is the second PC and consists of the second most significant common features and so on.

The waveforms in $\mathbf{A}$ can be reconstructed by taking a linear combination of PCs,

$$h_i \approx \sum_{j=1}^{k} U_j \beta_j, \tag{7}$$

where h_i is the desired waveform from the catalog, U_j is the jth PC from the $\mathbf{U}$ matrix and β_j is the corresponding PC coefficient, which can be obtained by projection of h_i onto U_j. The sum of k PCs produces an approximation of the desired waveform since $k \leq m$.

E. Signal and noise models

For the analysis described here, two types of models are considered. The signal model M_s tests the presence of a signal waveform $h(\beta)$ in the data. Here, PCA is performed for each catalog (using SVD; see Sec. III D) and each waveform is parametrized by its PC coefficients (β). The Gaussian likelihood function for the signal model is

$$p(D|\beta, M_s) = \prod_{i=1}^{N} \frac{1}{\sigma_i\sqrt{2\pi}} \exp\left[-\frac{(D_i - h_i(\beta))^2}{2\sigma_i^2}\right], \tag{8}$$

where σ_i is the standard deviation of the noise, $h_i(\beta)$ is the desired waveform reconstructed from the PCs and N is the length of the data with a corresponding index i. The evidence for the signal model is determined by performing the integral in Eq. (2) numerically, using uniformly-distributed priors over a chosen range for β.

On the other hand, the noise model M_n tests the data's consistency with Gaussian noise. The likelihood function for the noise model is the same as that in Eq. (8), but with $h(\beta) = 0$. From this, it is straightforward to perform the integration in Eq. (2) and obtain an analytic form for the noise evidence function,

$$p(D|M_n) = \prod_{i=1}^{N} \frac{1}{\sigma_i\sqrt{2\pi}} \exp^{-((D_i^2)/(2\sigma_i^2))}. \tag{9}$$

In both Eqs. (8) and (9), the standard deviation of the noise is a function of each sample in the data, because the simulated noise is designed to correspond to the expected sensitivity of Advanced LIGO, which varies as a function of frequency (see Sec. III F). To handle the frequency-dependent noise, the signal and noise evidences are calculated in the frequency domain with D_i, $h_i(\beta)$, and σ_i corresponding to data, reconstructed waveform, and noise in the ith frequency bin, respectively. In particular, each reconstructed waveform is obtained by taking a linear combination of the Fourier transforms of its corresponding PCs.

The natural logarithm of the Bayes factor used to compare the signal model to the noise model is then simply

$$\log B_{\mathrm{SN}} = \log[p(D|M_s)] - \log[p(D|M_n)]. \tag{10}$$

F. Generation of simulated noise

We generate Gaussian colored noise, assuming a single Advanced LIGO detector in the proposed broadband configuration (the so-called "zero detuning, high-power" mode). We employ the data file ZERO_DET_HIGH_P.TXT provided by [113], which contains $\sqrt{S(f)}$, the square root of the one-sided detector noise power spectral density in units of $(\mathrm{Hz})^{-1/2}$. An open-source implementation for MATLAB of what we describe in the following can be found in [114].

The real discrete time-domain noise $n(t_j)$, where t_j denotes the jth discrete time interval of size Δt, is obtained by inverse discrete Fourier transform from the complex frequency-domain noise $\tilde{n}(f_k)$, where f_k denotes the kth discrete frequency interval of size $\Delta f = 1/(N_t \Delta t)$, where N_t is the number of intervals in the time domain. Since the time-domain noise is real and has zero mean, the frequency-domain noise must obey

$$\tilde{n}(-f) = \tilde{n}^*(f), \tag{11}$$

$$\tilde{n}(f = 0) = \tilde{n}(f = f_{\mathrm{Nyq}}) = \tilde{n}(f = -f_{\mathrm{Nyq}}) = 0. \tag{12}$$

Here, $f_{\mathrm{Nyq}} = 1/(2\Delta t)$ is the Nyquist frequency. If N_t is the even number of equally spaced bins in time of width Δt, then $N_f = N_t/2 - 1$ is the number of independent frequency bins f_k in the frequency domain of width Δf. The frequency variable f_k assumes values from $-f_{\mathrm{Nyq}}$ to f_{Nyq}.

$|\tilde{n}(f_k)| = \sqrt{\tilde{n}(f_k)\tilde{n}^*(f_k)}$ is a two-sided amplitude spectral density. We generate $\tilde{n}(f_k)$ by sampling the standard normal distribution (zero mean, variance one) weighted by the noise transfer function $T(f_k) = \sqrt{S(f_k)}/\sqrt{2}$. The real and imaginary parts of $\tilde{n}(f_k)$ are then given for each $f_k \in (0, f_{\rm Nyq})$ by

$$\mathbb{R}(\tilde{n}(f_k)) = \frac{1}{\sqrt{2}} T(f) \texttt{RANDN}, \tag{13}$$

$$\mathbb{I}(\tilde{n}(f_k)) = \frac{1}{\sqrt{2}} T(f) \texttt{RANDN}, \tag{14}$$

where RANDN is a random number sampled from the standard normal distribution. The remaining $\tilde{n}(f_k)$ are then obtained via Eqs. (11) and (12).

The inverse discrete Fourier transform of $\tilde{n}(f_k)$ to time domain noise $n(t_j)$ will preserve its Gaussian character in the time domain in the limit of small sampling interval [39,112]. Specifically, we use the following definition of the discrete Fourier transform (DFT) for transforming noise from the frequency to the time domain when needed:

$$\tilde{n}(f_k) = \sum_{j=0}^{N-1} n(t_j) \exp(-2\pi \mathrm{i} jk/N), \tag{15}$$

$$n(t_j) = \frac{1}{N} \sum_{k=0}^{N-1} \tilde{n}(f_k) \exp(2\pi \mathrm{i} jk/N). \tag{16}$$

For convenience, we define the matched filter signal-to-noise ratio (SNR) of a GW signal h as

$$\mathrm{SNR}^2 = 4 \int_0^\infty \frac{|\tilde{h}(f)|^2}{S(f)} df \tag{17}$$

$$= 4\Delta t^2 \Delta f \sum_{k=1}^{N_f} \frac{|\tilde{h}(f_k)|^2}{S(f_k)}, \tag{18}$$

where $S(f)$ is the one-sided noise power spectral density. The factor Δt^2 is applied to correct the dimensions of $\tilde{h}(f)$, which we obtain via the DFT defined by Eq. (15).

G. Application in SMEE

1. GW signal preparation and PCA

Before carrying out PCA and injecting signals into noise, all waveforms are buffered with zeros to be of length n, which we choose to correspond to 3 S at a sampling rate of 4096 Hz, allowing us to comfortably accommodate the longest available core-collapse supernova GW signals. The Advanced LIGO sampling rate is 16 kHz. The reduced sampling rate we choose saves computation time and is sufficient to capture the frequency content of the core-collapse supernova waveforms considered here, which have most of their power at ~50–1000 Hz.

We align waveforms from the DIM catalog at their maximum (the spike at core bounce). Waveforms from the MUR and OTT catalogs are aligned so that the onsets of emission coincide. All waveforms are shifted so that they are aligned to the 4000th point in the SMEE input data file, corresponding to about the 1 S mark in the 3 S interval, to leave ample space left and right of the waveform.

In Fig. 3, we present the first three PCs computed for the DIM (magnetorotational mechanism; left panel), MUR (neutrino mechanism; center panel), and OTT (acoustic mechanism; right panel) catalogs. Before generating PCs for the MUR catalog we filter out the secular low-frequency drifts present in the MUR waveforms (see Fig. 1) by high-passing the signal above 30 Hz. Since the low-frequency components are hidden in detector noise even when the source is nearby, dropping them improves the efficiency of our subsequent Bayesian analysis and signal reconstruction. We apply the same high-passing to trial waveforms for the neutrino mechanism before injecting them into noise.

2. Signal injection and model selection

We inject trial GW signals into simulated Gaussian Advanced LIGO noise and use SMEE to determine which signal model (e.g., what core-collapse supernova explosion mechanism) a given injected signal belongs to via the evaluation of the logarithmic Bayes factors $\log B_{SN}$ [Eq. (10)] for an injected signal for each signal model S and the noise model N. Comparing two signal models i and j is then accomplished by computing $\log B_{ij} = \log B_{iN} - \log B_{jN}$.

SMEE's model selection operates in the frequency domain. Trial GW signal and the PCs belonging to the signal model under consideration are transformed into the frequency domain via DFT and the trial GW signal is added to the complex frequency-domain noise, retaining phase information. The nested sampling algorithm is then invoked to marginalize the PC coefficients β_k. The prior for each coefficient is flat and uniform. The prior range for each β_k is determined by first reprojecting all waveforms of a given catalog back onto the PCs to compute $\hat{\beta}_{kl}$ for each PC k and waveform l of the catalog. The range of expected possible values of β_k is then found by taking the minimum and maximum of $\hat{\beta}_{kl}$ over all l and adjusting these numbers by 10% down and up to add a margin of error to account for uncertainty due to the noise, motivated by the findings of [39].

Keeping the noise model fixed, the results of SMEE's computations will depend on the SNR of the signal, i.e. the distance to the core-collapse event, and on the amount of information we can provide to SMEE about expected signals in the form of PCs.

The maximum number of PCs at SMEE's disposal is limited by the number of waveforms used to determine the

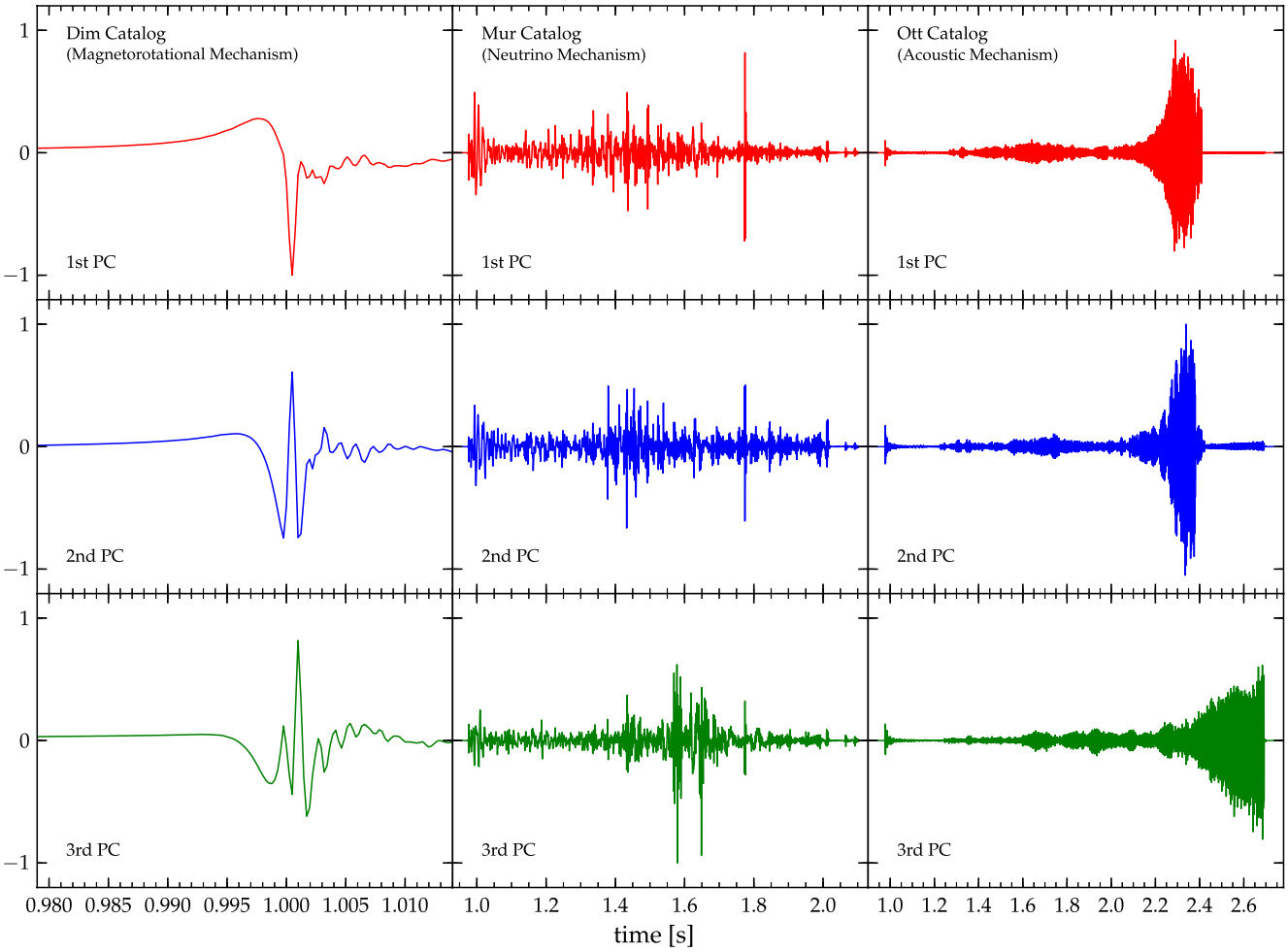

FIG. 3 (color online). The first three PCs of the waveforms from the DIM [17,100], MUR [73,84], and OTT [12,84] catalogs, which we take to be representative of the magnetorotational, neutrino and acoustic mechanisms, respectively (see Secs. II A, II B, and II C). In creating the PCs, the waveforms of each catalog are placed in a systematic way in a 3 s interval and padded left and right by zeros. The vertical axis is a dimensionless scale which represents the amplitude, which we have normalized by the maximum amplitude over all 3 PCs of each catalog shown here.

set of PCs. While each catalog used in this study has a different number of waveforms, we choose to simplify our analysis by using the same number of PCs for all catalogs. Hence, the maximum number of PCs we use here is 7 and is set by the number of waveform in the OTT catalog (see Sec. II C 1). Using 7 PCs gives SMEE complete information about signals belonging to the OTT catalog and significant, but incomplete information about waveforms from the DIM, MUR, and ABD catalogs. We also carry out SMEE runs with less than 7 PCs to study the dependence on the number of PCs employed. Using only a small subset of a catalog's PCs limits SMEE's ability to precisely reconstruct injected catalog waveforms, but it represents the real-life situation that the a priori information about a detected signal is severely limited. Our goal here is not to ideally reconstruct signals but to show that determining the underlying physical model of an observed signal is possible with limited advance knowledge.

IV. RESULTS

A. Response to Gaussian noise

For interpreting the results of SMEE's Bayesian model selection on the basis of Eq. (3), it is necessary to quantify and understand SMEE's response to pure Gaussian detector noise without a signal being present. To this end, we run SMEE on 10,000 randomized instances of Advanced LIGO detector noise (generated as described in Sec. III F) without injecting signals and compute $\log B_{SN}$ [Eq. (10)] in the absence of a signal for each signal model S. The results, shown in Fig. 4, follow a Gaussian distribution with a mean corresponding to the expected value $-\sum_{i=1}^{N}([h_i(\beta)^2]/[2\sigma_i^2])$, where N is the number of PCs employed (see Sec. III E). The average logarithmic Bayes factors obtained for 10,000 instances of noise indicate that noise, or any signal fully consistent with noise, is most likely to have a logarithmic Bayes factor of -54.0 when

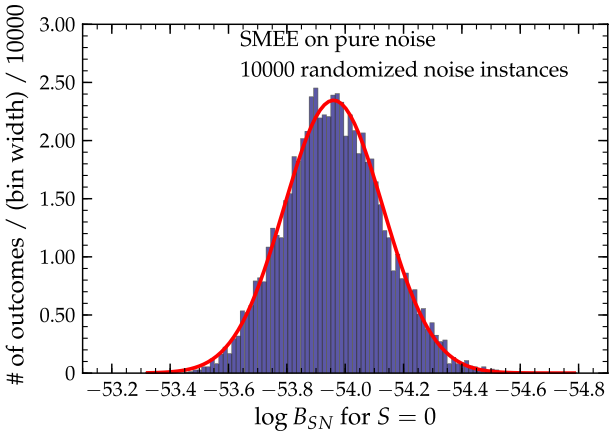

FIG. 4 (color online). Results from running SMEE with 7 PCs of the DIM catalog and without an injected signal on 10,000 randomized instances of Gaussian Advanced LIGO noise, generated as described in Sec. III F. A signal consistent with noise is most likely to have a logarithmic Bayes factor of ~ -54.0. The red line plots a Gaussian distribution with a mean of -53.96 and a standard deviation $\sigma = 0.17$.

SMEE is run with 7 PCs of the DIM catalog. For the OTT, MUR, and ABD catalogs, the expected logarithmic Bayes factors for pure Gaussian noise and 7 PCs are -52.1, -52.3, and -53.0, respectively. The observed expectation values are very comparable to those calculated for the DIM (-53.9), OTT (-52.2), MUR (-52.3), and ABD (-52.9) catalogs, respectively, verifying that SMEE is operating as expected. We have repeated this experiment for the case when only 3 PCs are used and also in this case find that SMEE closely reproduces the predicted expectation values, which are near -26 in the 3-PC case.

Since the logarithmic Bayes factors follow a Gaussian distribution, we can set a threshold using the standard deviations as an indicator for the expected false alarm rate. Ideally, for the DIM catalog, a 1% false alarm rate would correspond to a threshold that is ~ 2.6 times the standard deviation, corresponding to ~ 0.44 above the mean. However, we note that the expected logarithmic Bayes factor value varies between different catalogs and, for a fixed false alarm rate, we would require a different threshold for each catalog. This variation can be address by renormalizing all Bayes factors so that they are the same for all catalogs when there is only noise. But, since the focus of our work here is to distinguish between different waveforms and not to perform a study on the detection efficiency of GW signals, we choose to take the more conservative approach of simply setting a higher threshold. Therefore, we conservatively choose to identify a signal as being distinct from noise if its $\log B_{SN}$ is greater than -47 (in cases in which we use 3 PCs, this number is -21). When comparing two signal models M_i and M_j, we conservatively identify model M_i as favored if $\log B_{ij} \geq 5$ (and vice versa).

B. Signal versus noise

The minimal GW signal strength required for SMEE to be able to select the core-collapse supernova mechanism is an important question. The primary prerequisite for an incident GW signal to be useful for model selection is that SMEE can distinguish it from detector noise, i.e., we must find the minimum signal strength (i.e., SNR) so that $\log B_{SN} > -47$ [when 7 PCs are used; Eq. (10) and Sec. IV A].

In order to determine the range of minimum SNR required across and within core-collapse supernova GW signal types, we draw 5 representative waveforms from the DIM, MUR, and OTT catalogs and run them through SMEE at varying SNR, using 7 PCs generated from the catalog to which each injected waveform belongs. We choose the waveforms in such a way to capture the full range of variation within each catalog. The result of this exercise is shown in Fig. 5 and summarized in Table I. Generally, an SNR $\gtrsim 4-5$ is required for SMEE to find $\log B_{SN} > -47$ in the idealized setting that we consider here. In a real fully blind search, unknown arrival times and non-Gaussianity of real detector noise will generally require an SNR in excess of 8 for a detection statement (e.g., [115]).

In Fig. 5, the waveforms associated with the acoustic mechanism (OTT catalog) require the smallest SNR,

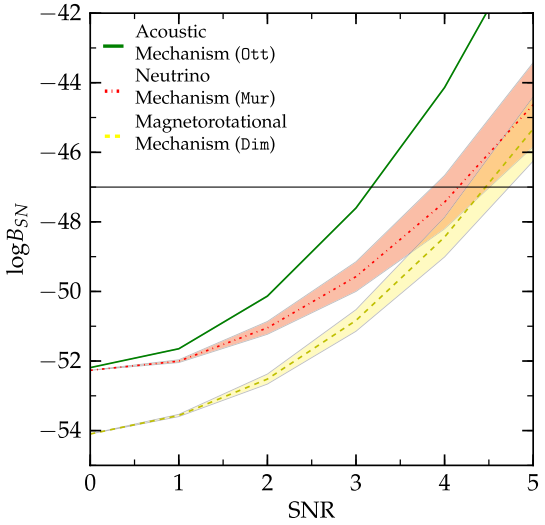

FIG. 5 (color online). Mean $\log B_{SN}$ as a function of signal-to-noise ratio [SNR; Eq. (18)] for 5 representative waveforms from the MUR, OTT, and DIM catalogs that encapsulate the variations within each catalog using 7 PCs. The shaded areas represent the standard error in the mean value of $\log B_{SN}$ for each waveform catalog computed as $\sigma = \pm N^{-1}(\Sigma_i(\bar{x} - x_i)^2)^{1/2}$, where $\bar{x}$ is the mean and x_i are the individual SNRs and N is the number of waveforms. Values of $\log B_{SN}$ below -47 in the 7-PC case and below -21 in the 3-PC case indicate that the algorithm considers it more likely that there is no signal detectable in the noise. Table I summarizes numerical results for the minimum SNR for which $\log B_{SN} \geq -47$.

followed by those of the neutrino mechanism (MUR catalog) and the magnetorotational mechanism (DIM catalog). This hierarchy in minimum SNR, however, is not fundamental, but a consequence of the fact that we have chosen to carry out this test using 7 PCs for each waveform catalog. Since the OTT catalog comprises only 7 waveforms, the set of 7 PCs completely spans it and allows perfect reconstruction, maximizing $p(D|M_s)$ [Eq. (8)]. In the case of less than perfect knowledge of the signal, the minimum SNR will always be greater. This is why the DIM and MUR catalogs, which have many more than 7 waveforms, require larger minimum SNR than the OTT waveforms.

The situation is somewhat different, when we recalculate $\log B_{SN}$ using only 3 PCs. The OTT catalog is very small and rather diverse in the time domain. Its first few PCs do not efficiently span the catalog and, when only the first 3 PCs are used, the minimum SNRs for waveforms poorly reconstructed with these PCs increases dramatically, as shown for the OTT waveforms nomoto13 and nomoto15 in Table I. Some of the MUR waveforms also exhibit increased minimum SNRs, indicating that there is significant time-domain variation that is not captured by the first 3 PCs. The large DIM catalog, on the other hand, is very efficiently spanned already by its first few PCs, as previously pointed out by [36,39], and the minimum SNR for waveforms from this catalog remains practically unchanged when going from 7 to 3 PCs in our analysis.

TABLE I. Minimum SNR at which the injected waveform will give a $\log B_{SN}$ above the threshold defined in Sec. IV A. This is shown for 5 representative waveforms from the DIM, MUR, and OTT catalogs, which we take to be representative of the magnetorotational, neutrino, and acoustic mechanisms, respectively. We provide results from SMEE runs with 3 and 7 PCs.

Waveform name	Minimum SNR	
	3 PCs	7 PCs
DIM [17]		
s11a1o01_Shen	13	13
s11a3o09_Shen	4	4
s20a3o05_LS	5	5
s40a3o07_LS	4	4
s40a3o13_Shen	4	4
MUR [73]		
20_3.8	9	4
40_10.0	4	4
40_13.0	21	15
15_3.2	10	9
15_4.0	4	4
OTT [12]		
nomoto13	143	4
nomoto15	45	4
s15.0WHW02	4	4
s20.0WHW02	4	4
s25.0WHW02	4	4

C. Determining the core-collapse supernova explosion mechanism

The basic assumption of this study is that the neutrino, magnetorotational, and acoustic core-collapse supernova explosion mechanism have robustly distinct GW signatures. In this section, we test this assumption by injecting waveforms into simulated noise and running SMEE on the data using PCs of waveform catalogs representative of the neutrino, magnetorotational, and acoustic mechanisms. If our assumption is correct and the GW signatures of these mechanisms are truly distinct, then SMEE should (i) yield the largest value of $\log B_{SN}$ when the set of PCs is used that corresponds to the mechanism the waveform is representative of, and, (ii) $\log B_{ij}$ [Eq. (3)] should be positive (and larger than $\sim$5; see Sec. IV A) if the injected waveform is most consistent with mechanism i, negative if it is most consistent with mechanism j, and near zero if the result is inconclusive.

We carry out our SMEE calculations for events located at 0.2, 2, and 10 kpc and with 3 and 7 PCs. Betelgeuse (α Orionis), a red supergiant star of 15–20$M_\odot$ [116], is located 197 $\pm$ 45 pc from Earth [117] and will eventually explode as a Type II-P core-collapse supernova. Hence, studying a potential event at 0.2 kpc will tell us what we can learn from the observation of GWs from Betelgeuse's collapse and supernova. 2 kpc is still nearby on the galactic scale, but the galactic volume out to this radius already contains hundreds of supergiants, one of which may make the next galactic supernova [118]. Finally, 10 kpc is the fiducial galactic distance scale and we consider it to state what could be inferred throughout the Milky Way. As in Sec. IV B, we carry out SMEE runs with 3 and 7 PCs to study the sensitivity of the results on the amount of knowledge about the injected waveform we grant SMEE.

Table II summarizes the results from $\log B_{SN}$ calculations for five representative waveforms from the MUR (neutrino mechanism), DIM (magnetorotational mechanism), and OTT (acoustic mechanism) catalogs. The larger the value of $\log B_{SN}$, the greater the confidence that the data contain a signal consistent with the employed set of PCs. $\log B_{SN} \leq -47$ (for the 7-PC case; -21 in the 3-PC case) indicates that the signal is more consistent with noise. The results show that it is indeed possible to clearly associate any injected waveform with its catalog and, thus, select the explosion mechanism for a core-collapse supernova out to at least 2 kpc. However, at the galactic scale (10 kpc), a significant fraction of waveforms representative of the neutrino mechanism, due to their intrinsically low GW amplitudes, can be told apart from noise only marginally or are even most consistent with noise. Typical magnetorotational explosions and explosions driven by the acoustic mechanism are still clearly identifiable at 10 kpc. However, when the reduced set of 3 PCs is used, the OTT catalog, which is not well spanned by only 3 PCs, suffers most and two out of the five representative OTT waveforms are not

TABLE II. $\log B_{SN}$ with respect to the DIM, MUR, and OTT PCs computed for representative injected waveforms from the DIM, MUR, and OTT catalogs, which we take to be representative of the magnetorotational, neutrino, and acoustic explosion mechanism, respectively. Results for source distances of 0.2, 2, and 10 kpc are given. Each table entry shows the results for 3 PCs (to the left of the vertical divider) and the 7-PC result (to the right of the divider). $\log B_{SN} < -47$ when 7 PCs are used and $\log B_{SN} < -21$ when 3 PCs are used indicates that the injected signal is likely consistent with noise while larger values suggests that the signal belongs to the signal model whose PCs were used in the analysis.

	$\log B_{SN}$ DIM PCs			$\log B_{SN}$ MUR PCs			$\log B_{SN}$ OTT PCs		
Waveform name	0.2 kpc	2 kpc	10 kpc	0.2 kpc	2 kpc	10 kpc	0.2 kpc	2 kpc	10 kpc
DIM [17]									
s11a1o01_Shen	38982|48686	364|430	−10| − 34	9178|25647	65|203	−22| − 42	−25|222	−27| − 51	−26| − 52
s11a3o09_Shen	5×10^6|5×10^6	52403|54505	2071|2129	36170|58531	335|532	−11| − 29	23|9191	−26|39	−26| − 49
s20a3o05_LS	3×10^6|3×10^6	25738|26859	1005|1023	4139|29285	15|240	−24| − 40	1|2242	−26| − 31	−26| − 51
s40a3o07_LS	1×10^7|1×10^7	1×10^5|1×10^5	4737|5411	47029|1×10^5	444|951	−7| − 12	519|56978	−21|517	−26| − 29
s40a3o13_Shen	2×10^7|2×10^8	2×10^5|2×10^5	8174|8302	2×10^5|4×10^5	1830|3968	48|109	160|19781	−25|145	−26| − 44
MUR [73]									
20_3.8	4205|10631	16|50	−24| − 50	59264|4×10^5	566|3775	−2|101	−22| − 5	−27| − 53	−26| − 52
40_10.0	280|2362	−23| − 33	−26| − 53	4×10^5|5×10^5	4198|4981	143|149	−26| − 29	−27| − 54	−26| − 52
40_13.0	365|819	−23| − 48	−26| − 54	3874|7591	12|23	−24| − 49	−27| − 42	−27| − 54	−26| − 52
15_3.2	7450|10699	48|51	−23| − 50	23744|29439	211|241	−16| − 41	−25| − 12	−27| − 53	−26| − 52
15_4.0	2030|7658	−6|20	−25| − 51	8×10^5|8×10^5	7672|7812	282|262	−12| − 22	−26| − 53	−26| − 52
OTT [12]									
nomoto13	3731|6155	11|4	−24| − 51	132|313	−25| − 50	−26| − 52	544|1×10^6	−21|11893	−26|426
nomoto15	1520|2428	−11| − 32	−25| − 53	54|146	−26| − 52	−26| − 52	32145|7×10^6	295|65635	−13|2575
s15.0WHW02	578|2417	−20| − 33	−26| − 53	1931|2601	−7| − 27	−25| − 51	6×10^7|6×10^7	6×10^5|6×10^5	24653|24655
s20.0WHW02	622|2895	−20| − 28	−26| − 53	−19|587	−27| − 47	−26| − 52	4×10^7|4×10^7	4×10^5|4×10^5	17975|17957
s25.0WHW02	2343|5963	−3|3	−25| − 51	1918|2969	−7| − 24	−25| − 51	1×10^8|1×10^8	1×10^6|1×10^6	45853|45829

or only marginally identifiable with the 3 first OTT PCs at 10 kpc.

Provided that there is confidence that a signal has been detected, we can compute $\log B_{ij}$ [Eq. (3)] to study if the signal is more likely to be consistent with mechanism i or mechanism j. Since we know $\log B_{SN}$ for all signal models, we can simply compute $\log B_{ij} = \log B_{iN} - \log B_{jN}$ from the data for representative waveforms provided in Table II. We use 7 PCs for these calculations.

In Fig. 6, we show results of injection studies of *all* waveforms from the DIM, MUR, and OTT catalogs run through SMEE and analyzed with the DIM, MUR, and OTT PCs at a source distance of 10 kpc. The full numerical results on whose basis Fig. 6 was generated are available

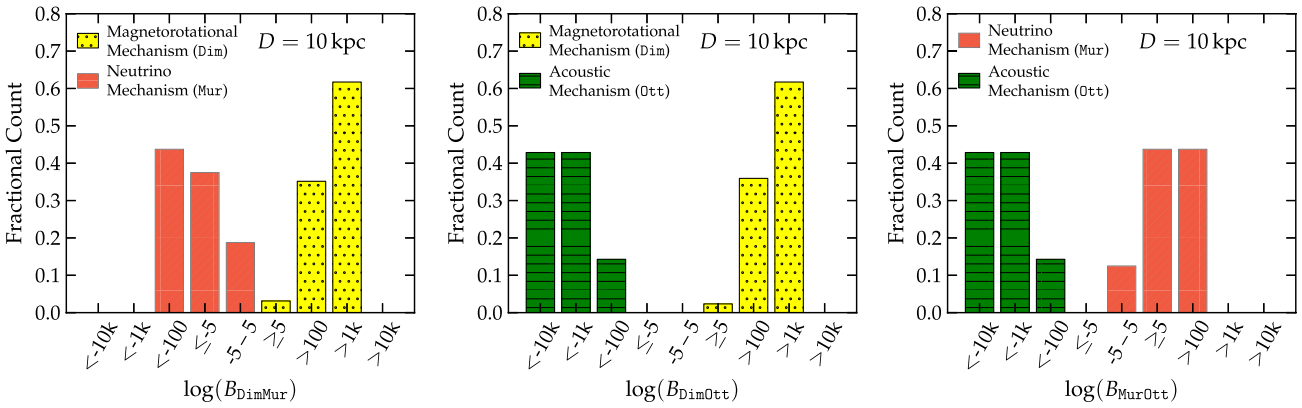

FIG. 6 (color online). Histograms describing the outcome of signal model comparisons by means of the Bayes factors $\log B_{ij} = \log p(D|M_i) - \log p(D|M_j)$, where $i \neq j$ and M_i and M_j are signal models described by the DIM (magnetorotational mechanism), MUR (neutrino mechanism), and OTT (acoustic mechanism) waveform catalogs. The Bayes factors are computed with 7 PCs and for a source distance of 10 kpc. A positive value $\log B_{ij}$ indicates that the injected waveform most likely belongs to model M_i, while a negative value suggest that model M_j is the more probable explanation. The bars are color-coded according to the type of injected waveform. The results are binned into ranges of varying size from < -10000 to >10000 and the height of the bars indicates what fraction of the waveforms of a given catalog falls into a given bin of $\log B_{ij}$. We consider the range of $(-5, 5)$ of $\log B_{ij}$ as inconclusive evidence (see Sec. IV A).

online [119]. The left panel depicts the $\log B_{\mathrm{DIMMUR}}$ result for injected waveforms from the DIM and MUR catalogs, that we take to be representative of the magnetorotational and neutrino mechanism, respectively. Even at 10 kpc the vast majority of waveforms characteristic for magnetorotational explosions are clearly identified as belonging to this mechanism. For the neutrino mechanism, the evidence is generally significantly weaker and only ∼44% of the MUR waveforms are identified with $\log B_{\mathrm{DIMMUR}} < -100$ and none have $\log B_{\mathrm{DIMMUR}} < -1000$, while ∼19% are in the inconclusive regime of $-5 < \log B_{\mathrm{DIMMUR}} < 5$.

In the center panel of Fig. 6, we show results for $\log B_{\mathrm{DIMOTT}}$ for injected waveforms corresponding to the magnetorotational (DIM) and the acoustic (OTT) mechanism. The case is clear cut and most waveforms are correctly identified as most likely belonging to their respective catalog/mechanism. Finally, the right panel of Fig. 6 presents $\log B_{\mathrm{MUROTT}}$ for waveforms representative of the neutrino (MUR) and acoustic (OTT) mechanism. As in the previous panel, SMEE associates the waveforms corresponding to the acoustic mechanism with high confidence to the OTT catalog. The evidence suggesting correct association of the neutrino mechanism waveforms is considerably less strong, but $\log B_{\mathrm{MUROTT}}$ is still conclusive for ∼88% of the MUR waveforms.

Figure 7 shows the results for $\log B_{\mathrm{DIMMUR}}$, $\log B_{\mathrm{DIMOTT}}$, and $\log B_{\mathrm{MUROTT}}$ obtained by SMEE with 7 PCs at a source distance of 2 kpc. Here, all acoustic mechanism waveforms (OTT catalog), all magnetorotational mechanism waveforms (DIM call), and all neutrino mechanism waveforms (MUR catalog) are correctly identified as belonging to their respective catalog and explosion mechanism.

D. Deciding between rotating accretion-induced collapse and rotating iron core collapse

The waveforms of the DIM catalog are representative of the GW signal emitted by rotating collapse and bounce of iron cores of massive stars with ZAMS masses $\gtrsim 8$–$10 M_\odot$. In the AIC of rapidly rotating O − Ne white dwarfs, very similar dynamics occurs and the corresponding GW signals, as predicted by Abdikamalov *et al.* [46], share many of the basic features of the rotating iron core collapse and bounce waveforms of, e.g., the DIM catalog (see the discussion in Sec. IV C of [46]). Hence, it is interesting to see if our SMEE model selection algorithm can tell them apart.

We compute the PCs for the ABD catalog in the same fashion as done previously for the DIM, MUR, and OTT catalogs and inject all ABD and DIM waveforms into simulated Advanced LIGO noise. Since the ABD and DIM catalogs are very similar, the results found for DIM waveforms in Sec. IV B carry over directly to ABD waveforms. SMEE is then run with 7 PCs to calculate $\log B_{\mathrm{ABDDIM}}$. The result is shown in Fig. 8 for source distances of 10 and 2 kpc. Full numerical results are available online [119].

In spite of the strong general similarity of rotating iron core collapse and rotating AIC waveforms, SMEE correctly identifies the vast majority of injected waveforms as most likely being emitted by a rotating iron core collapse or by rotating AIC. However, for a source at 10 kpc (left panel of Fig. 8), ∼6% of the DIM and ∼5% of the ABD are incorrectly identified as belonging to the respective other catalog. For an additional 2% of the DIM waveforms and 14% of the ABD waveforms, the evidence is inconclusive.

At a source distance of 2 kpc (right panel of Fig. 8), 88% of the AIC (ABD) and 93% of the rotating core-collapse (DIM) waveforms are correctly identified.

If one placed trust in the reliability of less dominant and more particular features of waveforms in the underlying catalogs, one could use a larger number of PCs in the analysis. In order to study the effect of using an increased number of PCs, we rerun the ABD vs. DIM comparison with 14 PCs and find that the result is significantly worse than with 7 PCs: ∼61% of the ABD waveforms and ∼23% of the DIM catalog are now incorrectly attributed to the respective other catalog at 10 kpc. This counterintuitive and at first surprising result is readily explained by the overall great similarity of the AIC and iron core-collapse waveforms and the nature of PCA and SMEE's Bayesian model selection. The most robust features of each waveform

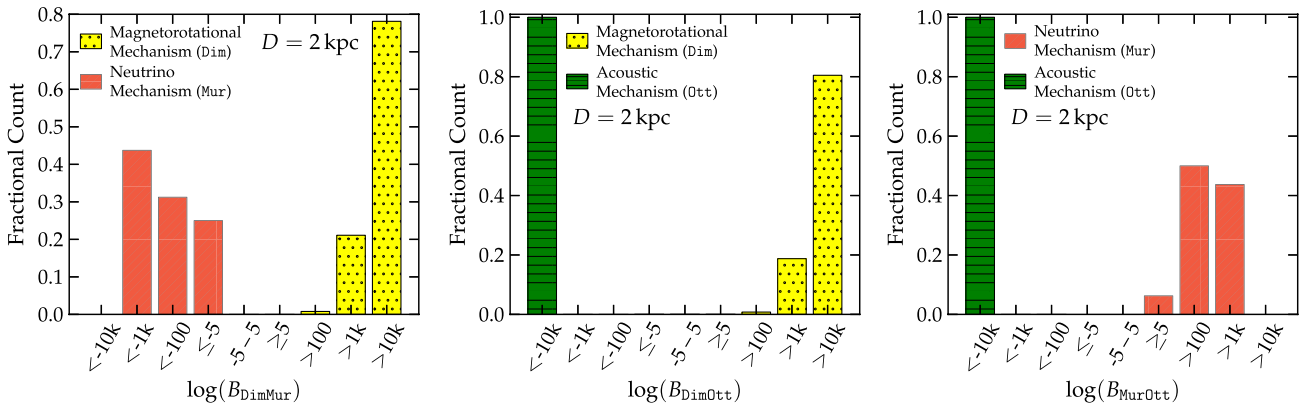

FIG. 7 (color online). Same as Fig. 6, but computed for a source distance of 2 kpc.

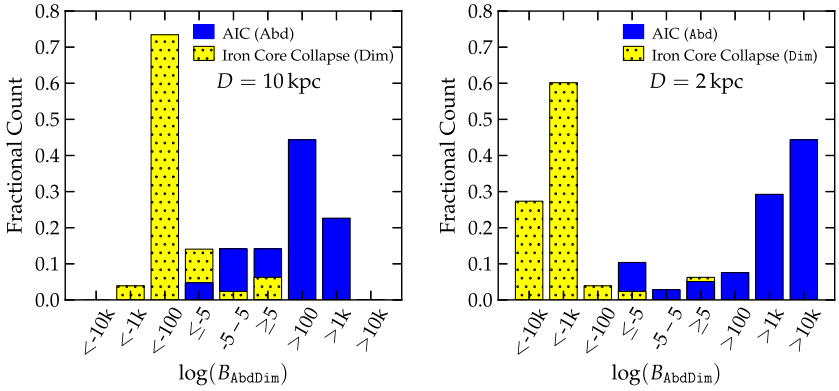

FIG. 8 (color online). Outcome of the SMEE analysis of injected rotating iron core collapse (DIM catalog) and rotating accretion-induced collapse (ABD catalog) waveforms. The left panel shows results for a source distance of 10 kpc and the right panel depicts the results for a distance of 2 kpc. The Bayes factors $\log B_{\mathrm{ABDDIM}}$ are computed on the basis of 7 PCs from the ABD and DIM catalog. A positive value of $\log B_{\mathrm{ABDDIM}}$ indicates that an injected waveform is most likely associated with rotating AIC and a negative value suggests it to be more consistent with rotating iron core collapse. The results are binned into ranges of varying size from < -10000 to >10000 and the height of the color-coded bars indicates what fraction of the waveforms of a given catalog falls into a given bin of $\log B_{\mathrm{ABDDIM}}$. We consider the range of $(-5, 5)$ of $\log B_{ij}$ as inconclusive evidence (see Sec. IV A).

catalog are encapsulated in its first few PCs. The first DIM and ABD PCs are indeed significantly different, but subsequent ABD and DIM PCs exhibit rather similar secondary features. Since each PC carries the same weight in SMEE's evidence calculation, including a larger number of PCs dilutes SMEE's judgment in this case and leads to the observed false identifications.

E. Testing robustness with unknown waveforms

In the previous sections, we have demonstrated SMEE's ability to identify an injected trial GW signal as belonging to a particular physical model (i.e., emission mechanism and/or explosion mechanism). In this, however, we have drawn the injected waveforms directly from the catalogs used to generate the PCs. In other words, we have given SMEE (limited) advance knowledge about the injected waveforms.

Here, we carry out a much more stringent test of SMEE's ability to select between models of the core-collapse supernova mechanism by injecting waveforms that were not employed in the initial PC generation and/or stem from completely independent catalogs.

1. Magnetorotational mechanism

For the magnetorotational mechanism, we employ three additional DIM waveforms (DIMEXTRA, Sec. II B 1) that were not included in the calculation of the DIM PCs. Furthermore, we inject waveforms from rotating models of the SCH catalog of Scheidegger *et al.* [102,107] (see Sec. II B 1). The results of the $\log B_{SN}$ calculation for the magnetorotational, neutrino, and acoustic mechanism signal models are summarized in Table III. DIMEXTRA waveforms are identified as being most consistent with the DIM catalog and, hence, the magnetorotational mechanism. This is true with high confidence when 3 or 7 PCs are used and for all DIMEXTRA signals out to distances $\gtrsim 10$ kpc.

The SCH waveforms were generated with a completely different numerical code and thus allow for a truly independent test of our approach in SMEE. Also, unlike the DIM waveforms, the SCH waveforms are based on 3D simulations. Hence, they are not linearly polarized. For consistency with our current approach, we neglect $h_\times$ and inject only h_+ as seen by an equatorial observer. Results of SMEE $\log B_{SN}$ calculations for all injected SCH waveforms are summarized in Table III. SMEE correctly identifies *all* injected SCH waveforms as indicative of magnetorotational explosions at a source distance of 2 kpc. At 10 kpc, still 91% of the injected SCH waveforms are attributed to the magnetorotational mechanism, which is an indication of the robustness of the GW signal associated with rapid rotation and magnetorotational explosions. The very few SCH waveforms that SMEE is not able to clearly associated with the magnetorotational mechanism have such weak SNRs that they are more consistent with noise than with any of the catalogs at 10 kpc.

2. Acoustic mechanism

We test SMEE's ability to identify core-collapse supernovae exploding via the acoustic mechanism by injecting the three OTTEXTRA waveforms (see Sec. II C 1). The results of this test are again summarized in Table III. They suggest that the *a priori* unknown OTTEXTRA waveforms can be identified as belonging to the acoustic mechanism out to 2 kpc with great confidence when 7 PCs are used in the analysis. At 10 kpc, the waveforms are still correctly attributed to the acoustic mechanism, but the evidence is much weaker in the 7-PC case while the waveforms are more consistent with noise when the analysis is performed with only 3 PCs. The OTTEXTRA 3 waveform, which is

TABLE III. $\log B_{SN}$ for gravitational waveforms that were not included in the catalogs used for PC computation. The DIMEXTRA, SCH, OTTEXTRA, and YAK waveforms are discussed in Sec. II. The MURREM waveforms are three randomly selected waveforms from the MUR catalog that were removed before re-computation of the MUR PCs. Results are shown for source distances of 0.2, 2, and 10 kpc and for evaluations using 3 PCs (to the left of the vertical divider) and 7 PCs (to the right of the divider). Larger values indicate stronger evidence that the waveform is matched to the model catalog from which the PCs were constructed. $\log B_{SN} < -47$ when 7 PCs are used and $\log B_{SN} < -21$ when 3 PCs are used indicates that the injected signal is likely consistent with noise, while larger values suggest that the signal belongs to the signal model whose PCs were used in the analysis.

Waveform	$\log B_{SN}$ DIM PCs			$\log B_{SN}$ MUR PCs			$\log B_{SN}$ OTT PCs		
name	0.2 kpc	2 kpc	10 kpc	0.2 kpc	2 kpc	10 kpc	0.2 kpc	2 kpc	10 kpc
DIMEXTRA [39]									
s20a1o05_shen	$3\times10^6\|3\times10^6$	28269|31142	1106|1194	$1\times10^5\|2\times10^5$	1429|2020	32|31	352|6515	−23|12	−26| − 49
s15a1o03_LS	$8\times10^6\|9\times10^6$	89606|95070	3560|3751	$2\times10^5\|3\times10^5$	1966|2593	54|54	384|40334	−22|350	−26| − 36
s40a1o10_LS	$2\times10^7\|2\times10^7$	$2\times10^5\|2\times10^5$	6832|7564	$3\times10^5\|1\times10^6$	2624|14076	80|513	142|13089	−25|78	−26| − 47
SCH [102]									
R1E1CA	20861|32817	182|271	−17| − 41	68|482	−26| − 48	−26| − 52	−27|68	−27| − 52	−26| − 52
R1E1CA_L	11631|13694	90|80	−21| − 48	−25| − 48	−27| − 54	−26| − 52	−27|19	−27| − 53	−26| − 52
R1E1DB	19285|25307	167|196	−18| − 44	63|438	−26| − 49	−26| − 52	−26|89	−27| − 52	−26| − 52
R1E3CA	27629|46426	250|408	−15| − 35	1| − 6	−26| − 53	−26| − 52	−23|160	−27| − 52	−26| − 52
R1STCA	8304|10006	57|44	−23| − 50	114|127	−25| − 52	−26| − 52	−27| − 33	−27| − 54	−26| − 52
R2E1AC	$4\times10^5\|4\times10^5$	3923|4273	132|120	1133|1602	−15| − 37	−25| − 52	−19|991	−26| − 43	−26| − 52
R2E3AC	$4\times10^5\|4\times10^5$	3566|3902	118|104	1151|1567	−15| − 38	−25| − 52	−18|578	−26| − 47	−26| − 52
R2STAC	$8\times10^5\|8\times10^5$	7504|7785	275|260	405|1301	−22| − 40	−26| − 52	−25|1463	−27| − 39	−26| − 52
R3E1AC	$3\times10^6\|4\times10^6$	28195|37420	1103|1445	7418|13743	48|84	−23| − 47	126|10015	−25|47	−26| − 48
R3E1AC_L	$2\times10^6\|3\times10^6$	19227|25641	744|974	10361|11138	77|58	−22| − 48	103|5089	−25| − 2	−26| − 50
R3E1CA	$2\times10^6\|3\times10^6$	20652|30427	801|1165	7590|13598	50|83	−23| − 47	183|7814	−24|25	−26| − 49
R3E1DB	$2\times10^6\|3\times10^6$	20722|30537	804|1170	10102|18050	75|127	−22| − 45	176|7438	−25|21	−26| − 49
R3E2AC	$2\times10^6\|3\times10^6$	24203|27271	943|1039	4575|12516	19|72	−24| − 47	32|7135	−26|18	−26| − 49
R3E3AC	$3\times10^6\|4\times10^6$	33975|39403	1334|1524	5493|8915	29|36	−24| − 49	107|13629	−25|83	−26| − 47
R3STAC	$5\times10^6\|5\times10^6$	47277|50486	1866|1968	13231|17583	106|122	−21| − 45	70|10361	−26|50	−26| − 48
R4E1AC	$9\times10^6\|1\times10^7$	$87917\|1\times10^5$	3492|4121	15672|26725	130|214	−20| − 42	584|39541	−20|342	−26| − 36
R4E1CF	$5\times10^7\|6\times10^7$	$5\times10^5\|6\times10^5$	21092|22361	$8\times10^5\|3\times10^6$	7543|31753	277|1220	$655\|1\times10^5$	−20|1434	−26|7
R4E1EC	$8\times10^6\|8\times10^7$	75553|82557	2997|3251	15653|31961	130|266	−20| − 39	315|34696	−23|294	−26| − 38
R4E1FC	$4\times10^7\|4\times10^7$	$4\times10^4\|4\times10^5$	16017|17730	$3\times10^5\|5\times10^5$	3140|5586	101|173	$643\|1\times10^5$	−20|1253	−26|0
R4E1FC_L	$8\times10^6\|1\times10^7$	83536|97750	3317|3859	16402|21202	138|159	−19| − 44	301|33112	−23|278	−26| − 39
R4STAC	$9\times10^6\|1\times10^7$	$94188\|1\times10^5$	3743|5146	45510|63122	429|578	−8| − 27	1310|37004	−13|317	−25| − 37
R5E1AC	$7\times10^6\|8\times10^6$	70290|78739	2787|3098	36378|45202	337|399	−11| − 34	232|34696	−24|294	−26| − 38
OTTEXTRA [22]									
m15b6	1663|2165	−10| − 35	−25| − 53	247|1212	−24| − 41	−26| − 52	427|27296	−22|220	−26| − 41
s11WW	1450|7562	19| − 25	−23| − 51	272|1594	−24| − 37	−26| − 52	1056|39024	−16|337	−25| − 36
s25WW	7455| − 50221	51|63	−23| − 49	$2\times10^5\|4\times10^5$	2279|3801	66|102	$1\times10^5\|1\times10^7$	$1075\|1\times10^5$	18|5236
MURREM [73]									
20_3.4	4253|9073	16|34	−24| − 50	15668|22046	130|167	−20| − 43	−21| − 32	−27| − 53	−26| − 52
12_3.2	1461|7459	−12|18	−25| − 51	7905|14088	53|88	−23| − 47	−25| − 47	−27| − 54	−26| − 52
15_3.2	7450|10699	48|51	−23| − 50	10862|17337	82|120	−22| − 45	−25| − 12	−27| − 53	−26| − 52
YAK [58]									
s12_matter	212|349	−24| − 53	−26| − 53	777|1257	−19| − 41	−26| − 52	−24| − 31	−27| − 53	−26| − 52
s15_matter	194|504	−24| − 52	−26| − 54	902|2071	−17| − 33	−26| − 51	−25|5	−27| − 53	−26| − 52
s25_matter	1099|1381	−15| − 43	−25| − 53	726|2080	−19| − 32	−26| − 52	−16| − 25	−26| − 53	−26| − 52

clearly identified at 10 kpc, has an extreme SNR of ~2530 at this distance, while the two other waveforms have SNRs of ~50. SMEE's difficulty is illustrated in the right panel of Fig. 9, which indicates that the OTTEXTRA waveforms reach the threshold of $\log B_{SN} \geq -47$ only for SNRs $\gtrsim 35$, whereas OTT waveforms are identified already at SNRs $\gtrsim 4$, if the full set of 7 PCs is used. This is a strong indication that the range of possible waveform features associated with the acoustic mechanism is not efficiently covered by the 7 PCs generated from the OTT catalog. This could simply be attributed to the very small number of waveforms in this catalog. However, when studying the OTT and OTTEXTRA waveforms, one immediately notes that the time between the first peak (associated with core bounce) and the second peak (the global maximum, associated with the nonlinear phase of the protoneutron star pulsations) varies significantly between waveforms. Since we compute PCs in the time domain, such large-scale features are imprinted onto the PCs and make it difficult to identify waveforms whose two peaks are separated by significantly different intervals. An alternative method that may work much better for waveforms of this kind is to compute PCs

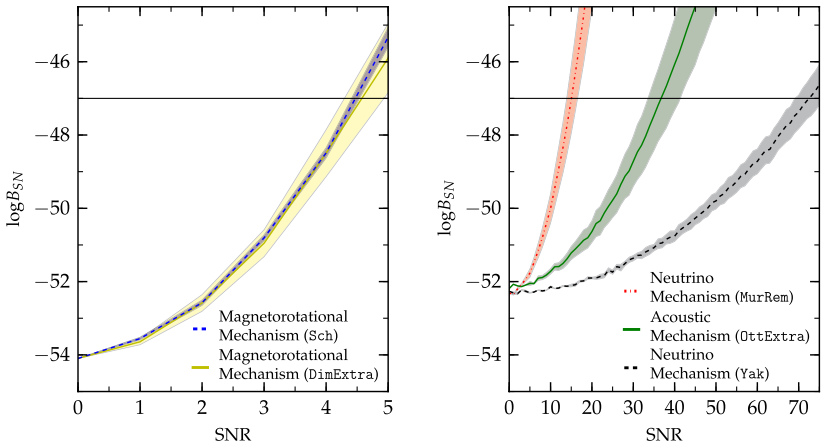

FIG. 9 (color online). Mean and 1-σ range of logB_{SN} as a function of signal-to-noise ratio SNR comparing signal with noise evidence. The horizontal lines mark the threshold values of logB_{SN} above which we consider an injected waveform to be distinct from Gaussian noise. *Left panel:* Results for the SCH and DIMEXTRA. These two were both reconstructed with 7 DIM PCs. *Right panel:* Results for the YAK, MURREM and OTTEXTRA waveforms as reconstructed with 7 MUR for the first two and 7 OTT PCs for the latter. The DIM PCs very efficiently reconstruct the SCH and DIMEXTRA waveforms at moderate SNRs while the YAK and OTTEXTRA require very high SNRs to be distinguished from noise by the MUR and OTT PCs, respectively.

based on waveform power spectra, which would remove any potentially problematic phase information.

3. Neutrino mechanism

We test SMEE's ability to identify GW signals emitted by core-collapse supernovae exploding via the neutrino mechanism in two ways. First, we remove three randomly selected MUR waveforms (MUR waveforms 20_3.4, 12_3.4, and 15_3.2, labeling this set as MURREM) from the MUR catalog, recompute the PCs without these 3 waveforms, then run SMEE to compute logB_{SN} for the three MURREM waveforms. The results, listed in Table III, show that SMEE is able to correctly identify MURREM waveforms as GW signals consistent with the MUR catalog with strong evidence out to a distance of ∼2 kpc and even at 10 kpc two out of three MURREM waveforms are picked out of the noise (though with relatively weak evidence). This is consistent with the overall results for waveforms belonging to the MUR catalog discussed in Sec. IV C.

However, a comparison of the right panel of Fig. 9 with Fig. 5 shows that the MURREM waveforms require an SNR that is more than twice as high to reach values of logB_{SN} at which we can consider them to be distinct from Gaussian noise. This is most likely due to the rather large diversity of MUR waveforms. Components of relevance to the MURREM waveforms are apparently not captured in the first 7 PCs when these waveforms are not included in the PCA.

A yet more stringent test is enabled by the waveforms of the YAK catalog (see Sec. II A) that were obtained with a completely different numerical code. We inject the three available YAK waveforms into Advanced LIGO noise and run SMEE on them to compute logB_{SN}. We list the results in Table III. SMEE correctly and clearly associates the YAK waveforms with the MUR PCs at 0.2 kpc. At 2 kpc, the association is still possible, but at 10 kpc the YAK waveforms appear to be most consistent with noise for SMEE. The right panel of Fig. 9 shows that the YAK waveforms require an SNR to be clearly associated with the neutrino mechanism that is $\gtrsim$7 times higher than for MURREM waveforms and more than ∼17 times higher than for MUR waveforms. This rather disappointing result can be explained as follows: while the YAK waveforms are qualitatively very similar to the MUR waveforms, they differ significantly in quantitative aspects. The YAK waveforms are generally only half as long (∼1 s for MUR and 0.5 s for YAK, whose models explode much earlier than the MUR models). Furthermore, the YAK waveforms have considerably more power at frequencies above ∼800 Hz and their energy spectra peak at ∼1000 Hz while most of the emission in the MUR waveforms occurs at or below ∼400 Hz. This may be due to the more simplified treatment of gravity and neutrino microphysics and transport in the study of Murphy *et al.* [73] underlying the MUR catalog compared to the work of Yakunin *et al.* [58] that led to the YAK catalog.

V. SUMMARY AND DISCUSSION

In this article, we have described the supernova model evidence extractor, a novel Bayesian approach to inferring physical information from observations of GW bursts emitted in stellar collapse and core-collapse supernovae. SMEE decomposes catalogs of simulated GW signals into their principle components and employs the nested sampling algorithm to compute the evidence that a trial signal injected into GW detector noise belongs to a given catalog.

It is evident that core-collapse supernovae are powered by the release of gravitational energy in gravitational collapse, but the central unsolved problem of core-collapse

supernova theory is by what mechanism this energy is transferred from the collapsed core to the stellar mantle to drive the explosion. Simulations show that multidimensional GW-emitting dynamics is a crucial ingredient to all potential explosion mechanisms. Hence, GWs could be ideal probes for the core-collapse supernova mechanism, provided that different mechanism models have clearly distinct GW signatures. In this paper, we have considered (i) the neutrino mechanism, (ii) the magnetorotational mechanism, and (iii) the acoustic mechanism for core-collapse supernova explosions and have treated mechanism as equally probable (i.e., having the same prior probability). The primary and dominant multidimensional dynamics and GW emission processes of these mechanisms are, ordered in the above order of mechanisms, (i) convection/turbulence and accretion downstreams, (ii) rapid rotation, and (iii) protoneutron star core pulsations, respectively.

Using GW signal catalogs based on simulations representative of these three mechanisms, we have applied SMEE to infer the explosion mechanism underlying trial waveforms injected into simulated Advanced LIGO noise. Our results show that our Bayesian approach is capable of identifying any of the considered explosion mechanisms with high confidence for core-collapse events occurring out to a distance of ~ 2 kpc even with only rudimentary knowledge of the precise shape of the expected signal.

Magnetorotational explosions, leading to particularly strong GW signals with very robust common features, can be clearly identified throughout the Milky Way ($D \gtrsim 10$ kpc). Our results also suggest that it is possible to further distinguish between rapidly rotating accretion-induced collapse of massive white dwarfs and rapidly rotating iron core collapse for events occurring in the galaxy, provided that the differences between the GW signals predicted by current simulations of rotating accretion-induced collapse and rotating iron core collapse are reliable.

GW signals emitted by neutrino-driven explosions have systematically lower amplitudes and, hence, are harder to distinguish from detector noise. Moreover, GW emission from convection/turbulence and accretion downstreams has not been as extensively studied, the available number of model waveforms is an order of magnitude smaller, and the currently predicted GW signals are not as reliable as in the case of rapidly rotating collapse. This reduces the efficacy of the principal component decomposition and, combined with the overall weakness of the signals, limits SMEE's robust reach for the neutrino mechanism to $\lesssim 2$ kpc for the currently available set of model waveforms and Advanced LIGO in broadband configuration.

The GW signals from core-collapse supernovae driven by the acoustic mechanism are strong and would likely be detectable by Advanced LIGO throughout the Milky Way. However, the set of available model waveforms for this signal type is very limited and individual waveforms differ significantly at large scales in the time domain while having similar frequency content. The inclusion of phase information (by computing PCs in the time domain and using their full complex Fourier transforms) in the current incarnation of SMEE is suboptimal for such signals and the PCs only inefficiently span the space of possible waveforms. This makes it difficult for SMEE to clearly identify the acoustic mechanism for core-collapse events occurring at distances significantly greater than ~ 2 kpc.

This study is the first systematic attempt at inferring core-collapse supernova physics from observations of GW bursts emitted by multiple different underlying mechanisms. While this is a significant step beyond previous work that focused only on GWs from rotating core collapse [32,39], our present study still suffers from a number of simplifying assumptions: we have considered only a single detector, Gaussian noise, and linearly polarized, optimally oriented GW emission. Real core-collapse supernovae will emit in both GW polarizations and will have arbitrary, generally nonoptimal orientation with respect to observatories on Earth. Advanced LIGO class GW detectors will operate as networks and observations will be coincident between three or even four detectors, and the noise backgrounds of these detectors will not be stationary and Gaussian, but nonstationary and glitchy. We have also been agnostic with regard to the prior probability of the three considered core-collapse supernova mechanisms. Input from astronomical observations and theory could be used to generate (approximate) prior probabilities for each mechanism, which could then be included in a future analysis.

Near future work on SMEE will be directed towards incorporating detector networks, variations in detector configurations and sensitivities, both GW polarizations, non-Gaussian noise, arbitrary source—detector orientations, and improved principal component analysis with and without reliance on the signal phase. However, even with these improvements, successful extraction of physics from core-collapse supernova GW signals will crucially depend on the availability of extensive catalogs of reliable predictions for both h_+ and $h_\times$. These must be provided by the core-collapse supernova modeling community on the basis of full 3D simulations.

ACKNOWLEDGMENTS

We thank the Basel, MPA Garching, ORNL, and Princeton core-collapse supernova modeling groups for making their gravitational waveforms publicly available. We are happy to acknowledge helpful exchanges with E. Abdikamalov, A. Burrows, Y. Chen, D. Chernoff, N. Christensen, T. Loredo, J. Murphy, J. Nordhaus, L. Santamaria, B. Schutz, M. Vallisneri, A. Weinstein, S. Wesolowski, and the core-collapse supernova working

group of the LIGO Scientific Collaboration and the Virgo Collaboration. C. D. O. is supported in part by the Sherman Fairchild Foundation and by the National Science Foundation under Grant No. PHY-0904015. Some of the results presented in this article were obtained through computations on the Caltech compute cluster "Zwicky" (NSF MRI Award No. PHY-0960291), on the NSF Teragrid under Grant No. TG-PHY100033, on machines of the Louisiana Optical Network Initiative under Grant No. loni_numrel07, and at the National Energy Research Scientific Computing Center (NERSC), which is supported by the Office of Science of the U.S. Department of Energy under Contract No. DE-AC02-05CH11231. I. S. H. and J. L. gratefully acknowledge the support of the U.K. Science and Technology Facilities Council and the Scottish Universities Physics Alliance (SUPA).

[1] W. Baade and F. Zwicky, Proc. Natl. Acad. Sci. U.S.A. **20**, 259 (1934).
[2] H. A. Bethe, Rev. Mod. Phys. **62**, 801 (1990).
[3] H.-T. Janka, K. Langanke, A. Marek, G. Martínez-Pinedo, and B. Müller, Phys. Rep. **442**, 38 (2007).
[4] P. Goldreich and S. V. Weber, Astrophys. J. **238**, 991 (1980).
[5] A. Yahil, Astrophys. J. **265**, 1047 (1983).
[6] E. O'Connor and C. D. Ott, Astrophys. J. **730**, 70 (2011).
[7] L. Wang and J. C. Wheeler, Annu. Rev. Astron. Astrophys. **46**, 433 (2008).
[8] N. Smith *et al.*, Mon. Not. R. Astron. Soc. **420**, 1135 (2012).
[9] T. Lund, A. Marek, C. Lunardini, H.-T. Janka, and G. Raffelt, Phys. Rev. D **82**, 063007 (2010).
[10] T. D. Brandt, A. Burrows, C. D. Ott, and E. Livne, Astrophys. J. **728**, 8 (2011).
[11] K. Hirata, T. Kajita, M. Koshiba, M. Nakahata, and Y. Oyama, Phys. Rev. Lett. **58**, 1490 (1987).
[12] C. D. Ott, Classical Quantum Gravity **26**, 063001 (2009).
[13] K. Kotake, arXiv:1110.5107 [C.R. Phys. (to be published)].
[14] B. Müller, H.-T. Janka, and A. Marek, arXiv:1202.0815.
[15] E. Müller, H.-T. Janka, and A. Wongwathanarat, Astron. Astrophys. **537**, A63 (2012).
[16] K. Kotake, W. Iwakami-Nakano, and N. Ohnishi, Astrophys. J. **736**, 124 (2011).
[17] H. Dimmelmeier, C. D. Ott, A. Marek, and H.-T. Janka, Phys. Rev. D **78**, 064056 (2008).
[18] T. Takiwaki and K. Kotake, Astrophys. J. **743**, 30 (2011).
[19] A. Marek and H.-T. Janka, Astrophys. J. **694**, 664 (2009).
[20] B. P. Abbott *et al.* (LIGO Scientific Collaboration), Rep. Prog. Phys. **72**, 076901 (2009).
[21] K. Kuroda (LCGT Collaboration), Classical Quantum Gravity **27**, 084004 (2010).
[22] C. D. Ott, A. Burrows, L. Dessart, and E. Livne, Phys. Rev. Lett. **96**, 201102 (2006).
[23] C. D. Ott, C. Reisswig, E. Schnetter, E. O'Connor, U. Sperhake, F. Löffler, P. Diener, E. Abdikamalov, I. Hawke, and A. Burrows, Phys. Rev. Lett. **106**, 161103 (2011).
[24] C. Fryer and K. C. B. New, Living Rev. Relat. **14**, 1 (2011).
[25] M. Punturo *et al.*, Classical Quantum Gravity **27**, 194002 (2010).
[26] B. J. Owen and B. S. Sathyaprakash, Phys. Rev. D **60**, 022002 (1999).
[27] A. C. Searle, P. J. Sutton, and M. Tinto, Classical Quantum Gravity **26**, 155017 (2009).
[28] Y. Gürsel and M. Tinto, Phys. Rev. D **40**, 3884 (1989).
[29] É. É. Flanagan and S. A. Hughes, Phys. Rev. D **57**, 4566 (1998).
[30] S. Klimenko, S. Mohanty, M. Rakhmanov, and G. Mitselmakher, Phys. Rev. D **72**, 122002 (2005).
[31] S. Klimenko, I. Yakushin, A. Mercer, and G. Mitselmakher, Classical Quantum Gravity **25**, 114029 (2008).
[32] T. Z. Summerscales, A. Burrows, L. S. Finn, and C. D. Ott, Astrophys. J. **678**, 1142 (2008).
[33] C. D. Ott, A. Burrows, E. Livne, and R. Walder, Astrophys. J. **600**, 834 (2004).
[34] P. R. Brady and S. Ray-Majumder, Classical Quantum Gravity **21**, S1839 (2004).
[35] T. Zwerger and E. Müller, Astron. Astrophys. **320**, 209 (1997).
[36] I. S. Heng, Classical Quantum Gravity **26**, 105005 (2009).
[37] K. V. Mardia, J. T. Kent, and J. M. Bibby, *Multivariate Analysis* (Academic Press, London, 1979).
[38] K. Cannon, A. Chapman, C. Hanna, D. Keppel, A. C. Searle, and A. J. Weinstein, Phys. Rev. D **82**, 044025 (2010).
[39] C. Röver, M.-A. Bizouard, N. Christensen, H. Dimmelmeier, I. S. Heng, and R. Meyer, Phys. Rev. D **80**, 102004 (2009).
[40] D. S. Sivia and J. Skilling, *Data Analysis: A Bayesian Tutorial* (Oxford University Press, Oxford, 2006), 2nd ed.
[41] A. Burrows, L. Dessart, E. Livne, C. D. Ott, and J. Murphy, Astrophys. J. **66**, 416 (2007).
[42] A. Burrows, E. Livne, L. Dessart, C. D. Ott, and J. Murphy, Astrophys. J. **640**, 878 (2006).
[43] A. Burrows, E. Livne, L. Dessart, C. D. Ott, and J. Murphy, Astrophys. J. **655**, 416 (2007).
[44] C. D. Ott,Classical Quantum Gravity **26**, 204015 (2009).
[45] J. Skilling, in *AIP Conference Proceedings: 24th International Workshop on Bayesian Inference and Maximum Entropy Methods in Science and Engineering*, edited by R. Fischer, R. Preuss, and U. V. Toussaint, Vol. 735, p. 395 (AIP Press, Garching, Germany 2004).
[46] E. B. Abdikamalov, C. D. Ott, L. Rezzolla, L. Dessart, H. Dimmelmeier, A. Marek, and H.-T. Janka, Phys. Rev. D **81**, 044012 (2010).
[47] C. D. Ott, E. P. O'Connor, and B. Dasgupta, in *Proceedings of the HAνSE 2011 Conference* (Institute

of Electrical and Electronics Engineers, Boca Raton, Florida, 2011).
[48] M. Hamuy, Astrophys. J. **582**, 905 (2003).
[49] W. D. Arnett, Can. J. Phys. **44**, 2553 (1966).
[50] S. A. Colgate and R. H. White, Astrophys. J. **143**, 626 (1966).
[51] H. A. Bethe and J. R. Wilson, Astrophys. J. **295**, 14 (1985).
[52] M. Liebendörfer, M. Rampp, H.-T. Janka, and A. Mezzacappa, Astrophys. J. **620**, 840 (2005).
[53] M. Rampp and H.-T. Janka, Astron. Astrophys. **396**, 361 (2002).
[54] T. A. Thompson, A. Burrows, and P. A. Pinto, Astrophys. J. **592**, 434 (2003).
[55] F. S. Kitaura, H.-T. Janka, and W. Hillebrandt, Astron. Astrophys. **450**, 345 (2006).
[56] R. Buras, H.-T. Janka, M. Rampp, and K. Kifonidis, Astron. Astrophys. **457**, 281 (2006).
[57] Y. Suwa, K. Kotake, T. Takiwaki, S. C. Whitehouse, M. Liebendörfer, and K. Sato, Publ. Astron. Soc. Jpn. **62**, L49 (2010).
[58] K. N. Yakunin, P. Marronetti, A. Mezzacappa, S. W. Bruenn, C.-T. Lee, M. A. Chertkow, W. R. Hix, J. M. Blondin, E. J. Lentz, O. E. Bronson Messer, and S. Yoshida, Classical Quantum Gravity **27**, 194005 (2010).
[59] C. D. Ott, A. Burrows, L. Dessart, and E. Livne, Astrophys. J. **685**, 1069 (2008).
[60] J. W. Murphy and A. Burrows, Astrophys. J. **688**, 1159 (2008).
[61] C. L. Fryer and M. S. Warren, Astrophys. J. **601**, 391 (2004).
[62] J. Nordhaus, A. Burrows, A. Almgren, and J. Bell, Astrophys. J. **720**, 694 (2010).
[63] T. Kuroda, K. Kotake, and T. Takiwaki, arXiv:1202.2487.
[64] W. Iwakami, K. Kotake, N. Ohnishi, S. Yamada, and K. Sawada, Astrophys. J. **700**, 232 (2009).
[65] T. Takiwaki, K. Kotake, and Y. Suwa, Astrophys. J. **749**, 98 (2012).
[66] F. Hanke, A. Marek, B. Müller, and H.-T. Janka, arXiv:1108.4355.
[67] J. M. Blondin, A. Mezzacappa, and C. DeMarino, Astrophys. J. **584**, 971 (2003).
[68] T. Foglizzo, P. Galletti, L. Scheck, and H.-T. Janka, Astrophys. J. **654**, 1006 (2007).
[69] T. Foglizzo, L. Scheck, and H.-T. Janka, Astrophys. J. **652**, 1436 (2006).
[70] L. Scheck, H.-T. Janka, T. Foglizzo, and K. Kifonidis, Astron. Astrophys. **477**, 931 (2008).
[71] E. Müller, M. Rampp, R. Buras, H.-T. Janka, and D. H. Shoemaker, Astrophys. J. **603**, 221 (2004).
[72] A. Marek, H.-T. Janka, and E. Müller, Astron. Astrophys. **496**, 475 (2009).
[73] J. W. Murphy, C. D. Ott, and A. Burrows, Astrophys. J. **707**, 1173 (2009).
[74] K. Kotake, N. Ohnishi, and S. Yamada, Astrophys. J. **655**, 406 (2007).
[75] C. L. Fryer, D. E. Holz, and S. A. Hughes, Astrophys. J. **609**, 288 (2004).
[76] K. Kotake, W. Iwakami, N. Ohnishi, and S. Yamada, Astrophys. J. Lett. **697**, L133 (2009).
[77] R. Epstein, Astrophys. J. **223**, 1037 (1978).
[78] A. Burrows and J. Hayes, Phys. Rev. Lett. **76**, 352 (1996).
[79] E. Müller and H.-T. Janka, Astron. Astrophys. **317**, 140 (1997).
[80] C. L. Fryer and A. Heger, Astrophys. J. **541**, 1033 (2000).
[81] R. Walder, A. Burrows, C. D. Ott, E. Livne, I. Lichtenstadt, and M. Jarrah, Astrophys. J. **626**, 317 (2005).
[82] S. A. Balbus and J. F. Hawley, Astrophys. J. **376**, 214 (1991).
[83] M. Obergaulinger, P. Cerdá-Durán, E. Müller, and M. A. Aloy, Astron. Astrophys. **498**, 241 (2009).
[84] C. D. Ott *et al.*, Gravitational Wave Catalog, http://www.stellarcollapse.org/gwcatalog.
[85] K. S. Thorne, in *300 Years of Gravitation,*, edited by S. W. Hawking and W. Israel (Cambridge University Press, Cambridge, 1987).
[86] A. Marek, H. Dimmelmeier, H.-T. Janka, E. Müller, and R. Buras, Astron. Astrophys. **445**, 273 (2006).
[87] Chimera Collaboration, ORNL/FAU Gravitational Wave Signal Catalog, http://astrodev.phys.utk.edu/chimera/.
[88] C. D. Ott, A. Burrows, T. A. Thompson, E. Livne, and R. Walder, Astrophys. J. Suppl. Ser. **164**, 130 (2006).
[89] A. Heger, S. E. Woosley, and H. C. Spruit, Astrophys. J. **626**, 350 (2005).
[90] J. C. Wheeler, I. Yi, P. Höflich, and L. Wang, Astrophys. J. **537**, 810 (2000).
[91] G. S. Bisnovatyi-Kogan, Astron. Zh. **47**, 813 (1970).
[92] K. Kotake, S. Yamada, K. Sato, K. Sumiyoshi, H. Ono, and H. Suzuki, Phys. Rev. D **69**, 124004 (2004).
[93] M. Obergaulinger, M. A. Aloy, H. Dimmelmeier, and E. Müller, Astron. Astrophys. **457**, 209 (2006).
[94] M. Shibata, Y. T. Liu, S. L. Shapiro, and B. C. Stephens, Phys. Rev. D **74**, 104026 (2006).
[95] L. Dessart, A. Burrows, E. Livne, and C. D. Ott, Astrophys. J. Lett. **673**, L43 (2008).
[96] P. Cerdá-Durán, J. A. Font, L. Antón, and E. Müller, Astron. Astrophys. **492**, 937 (2008).
[97] S. E. Woosley and A. Heger, Astrophys. J. **637**, 914 (2006).
[98] H. Dimmelmeier, C. D. Ott, H.-T. Janka, A. Marek, and E. Müller, Phys. Rev. Lett. **98**, 251101 (2007).
[99] C. D. Ott, H. Dimmelmeier, A. Marek, H.-T. Janka, I. Hawke, B. Zink, and E. Schnetter, Phys. Rev. Lett. **98**, 261101 (2007).
[100] H. Dimmelmeier, J. A. Font, H.-T. Janka, A. Marek, E. Müller, and C. D. Ott, MPA Garching Gravitational Wave Signal Catalog, http://www.mpa-garching.mpg.de/rel_hydro/wave_catalogue.shtml.
[101] S. Scheidegger, T. Fischer, S. C. Whitehouse, and M. Liebendörfer, Astron. Astrophys. **490**, 231 (2008).
[102] S. Scheidegger, R. Käppeli, S. C. Whitehouse, T. Fischer, and M. Liebendörfer, Astron. Astrophys. **514**, A51 (2010).
[103] M. Shibata and Y.-I. Sekiguchi, Phys. Rev. D **71**, 024014 (2005).
[104] M. Rampp, E. Müller, and M. Ruffert, Astron. Astrophys. **332**, 969 (1998).
[105] W. Fu and D. Lai, Mon. Not. R. Astron. Soc. **413**, 2207 (2011).
[106] M. Liebendörfer, Astrophys. J. **633**, 1042 (2005).
[107] S. Scheidegger, Gravitational Wave Catalogue, http://phys-merger.physik.unibas.ch/~simon/gw_data/.
[108] L. Dessart, A. Burrows, E. Livne, and C. D. Ott, Astrophys. J. **669**, 585 (2007).

[109] N. N. Weinberg and E. Quataert, Mon. Not. R. Astron. Soc. **387**, L64 (2008).
[110] M. Pitkin, S. Reid, S. Rowan, and J. Hough, Living Rev. Relat. **14**, 5 (2011).
[111] W. Del Pozzo, J. Veitch, and A. Vecchio, Phys. Rev. D **83**, 082002 (2011).
[112] J. Veitch and A. Vecchio, Phys. Rev. D **81**, 062003 (2010).
[113] D. Shoemaker (LIGO Collaboration), Report No. LIGO-T0900288-v3 (2010).
[114] LIGO Collaboration, Computer Code MATAPPS, http://ligo-vcs.phys.uwm.edu/wsvn/MatApps/packages/stochastic/trunk/PreProcessing/detectorNoise.m.
[115] J. Abadie *et al.* (LIGO Collaboration and VIRGO Scientific Collaboration), Classical Quantum Gravity **27**, 173001 (2010).
[116] N. Smith, K. H. Hinkle, and N. Ryde, Astron. J. **137**, 3558 (2009).
[117] G. M. Harper, A. Brown, and E. F. Guinan, Astron. J. **135**, 1430 (2008).
[118] M. M. Hohle, R. Neuhäuser, and B. F. Schutz, Astron. Nachr. **331**, 349 (2010).
[119] J. Logue, C. D. Ott, I. S. Heng, P. Kalmus, and J. Scargill, Inferring Core-Collapse Supernova Physics with Gravitational Waves, http://www.stellarcollapse.org/SMEE.